Peer-reviewed version available at *Materials* **2019**, *12*, 1744; doi:10.3390/ma12111744

Article

Enhanced Sol-Gel Route to Obtain a Highly Transparent and Conductive Aluminum-doped Zinc Oxide Thin Film

Mohammad Hossein Nateq [1,*] and Riccardo Ceccato [1]

[1] *University of Trento, Department of Industrial Engineering, University of Trento, Via Sommarive 9, 38123 Trento, Italy*
riccardo.ceccato@unitn.it
* Correspondence: mohammadhosein.nateq@unitn.it; Tel.: +39-3913113046

Received: date; Accepted: date; Published: date

Abstract: The electrical and optical properties of sol-gel derived aluminum-doped zinc oxide thin films containing 2 at.% Al were investigated considering the modifying effects of 1) increasing the sol H_2O content; and 2) thermal treatment procedure with high-temperature approach followed by an additional heat-treatment step under a reducing atmosphere. According to the results obtained via the TG-DTA analysis, FT-IR spectroscopy, X-ray diffraction technique and four-point probe resistivity measurement, it is argued that the sol hydrolysis, decomposition of the deposited gel and crystallization of grains result in grains of larger crystallite size and stronger c-axis preferred orientation with slightly less microstrain in the modified sample. The consequent morphology and grain-boundary characteristics turn out as improved conductivity, implying higher values of concentration and mobility of charge carriers. A detailed investigation on samples optical properties, in terms of analyzing their absorption and dispersion behaviors through the UV-Vis-NIR spectroscopy, support our reasoning for the increase of the mobility, and to a lesser extent, the concentration of charge carriers, while causing only a slight degradation of optical transmission. Hence, an enhanced performance as a transparent conducting film is claimed for the modified sample by comparing the figure-of-merit values.

Keywords: sol-gel; Al-doped ZnO; hydrolysis; thin film; transparent conductors; resistivity; UV-Vis-NIR spectroscopy; figure of merit

1. Introduction

Having high optical transmission together with low electrical resistivity is a unique feature exclusive to transparent conducting films (TCFs) affording them a number of specific applications in optoelectronic devices such as liquid crystal displays, light-emitting diodes, electromagnetic shielding of cathode-ray tubes, functional glasses, photoelectrochemical cells and sensors [1].

Among the limited number of materials possessing such a property, the most widely utilized are thin films of certain wide band-gap n-type semiconducting oxides like In_2O_3, SnO_2 and ZnO, known as transparent conducting oxides (TCOs). Here, non-stoichiometric excess of cations or oxygen vacancies can provide a considerable number of charge carriers, causing an intrinsically moderate but usually not sufficient electrical conductivity, which is significantly boosted when properly doped with appropriate elements [2]. However, due to the trade-off between electrical conductivity and optical transmission [3], the quality of a TCO is evaluated by a factor called figure-of-merit (FoM) to consider both properties simultaneously. For this purpose, it is necessary to measure average values of transmittance T, and sometimes reflectance R, generally within the visible wavelengths region, as well as the electrical sheet resistance, R_{sh}. Among different suggested definitions for FoM, the first successful one was defined by Haacke as $\mathrm{FoM} = T^{10}/R_{sh}$ [4], in which the dimension is Ω^{-1}, and a larger value indicates a better performance. With a similar dimension, a

Peer-reviewed version available at Materials 2019, 12, 1744; doi:10.3390/ma12111744

more practical definition was proposed by Jain and Kulshreshtha [3, 5], which evaluates the film performance independent of the thickness:

$$\mathrm{FoM} = -[\mathrm{R_{sh}}.\ln(\mathrm{T})]^{-1}. \quad (1)$$

This definition was later modified by Gordon [6], as $\mathrm{FoM} = -[\mathrm{R_{sh}}.\ln(\mathrm{T}+\mathrm{R})]^{-1}$ for applications such as low-emissivity windows equipped with infrared-reflecting glass [7], where the optical absorption is considered more decisive than the mere transmission. There is also a more sophisticated definition proposed by Gruner and modified by Coleman relying on a relationship in which, T and R_{sh} are correlated to σ_{DC}/σ_{OP} as the ratio of dc conductivity to the optical conductivity [8-10]. The derived equation [10] with a similar dimension to Haacke's FoM is:

$$\mathrm{FoM} = 188.5.[\mathrm{R_{sh}}.(\mathrm{T}^{-0.5}-1)]^{-1}. \quad (2)$$

The most commonly-used TCO material is indium tin oxide (ITO) since it offers the highest FoM value [11]. However, the global shortage and increasing price of indium has triggered attempts to enhance the properties of more affordable TCOs, especially Aluminum-doped ZnO (AZO) [13,14]. On an industrial scale, the deposition of AZO and other TCO films is usually performed through expensive vacuum-based technologies such as sputtering to obtain high-quality films. Another approach is using wet deposition techniques such as sol-gel method which provide a considerably more affordable way without the necessity of applying high temperature or vacuum condition [2]. They are also quite suitable for samples with sizable or non-flat surfaces like tubes [14]. In spite of such advantages, the sol-gel derived films are often porous and of lower quality and less FoM values than those of sputtered films [15], which necessitates further investigation to improve the sol-gel procedure. To date, the solution-based methods have been considered highly promising in inkjet printing of TCOs for low-cost printed electronics and solar cells [16].

In the sol-gel synthesis of thin films, nanocrystalline or amorphous as-deposited layers transform into the crystalline state by the post-deposition crystallization, throughout which the crystal orientation and grain-boundary characteristics develop. These microstructural features affect the optical and electrical properties and hence, the FoM value. Accordingly, controlling the film crystallization is a crucial step in the sol-gel synthesis of TCOs. Based on the barrier model theory proposed by Seto on the electrical properties of polycrystalline silicon films [17], and its expansion to AZO structures [18], Ohyama [19] and Nishio [20] concluded that AZO shows higher conductivity in the case of having a highly-oriented microstructure toward the c-axis of the zincite structure, compared with less-oriented or granular microstructures. Considering that the conductivity σ is in a direct relationship with the concentration N and mobility μ of charge carriers as $\sigma \sim \mathrm{N}.\mu$, a higher concentration results in less optical transmission, while the effect of the mobility value on transmission is insignificant [21]. Accordingly, a highly-oriented microstructure shows higher conductivity because the mobility of charge carriers is enhanced by grain-boundary scattering being less effective. Higher conductivity is thus obtained while the optical transmission is unaffected, which mean a higher FoM value. Heretofore, many attempts have been devoted to improve the performance of the sol-gel derived AZO thin films through studying how microstructural features are influenced by processing parameters, including solvent and stabilizer types [23-26], precursor and doping concentrations [23,20,27], deposition conditions [20,26], the drying temperature [20,28, 29] and finally annealing cycles and atmosphere [20,30,31]. However, to the best of our knowledge, these studies have focused on each parameter independently and there is no investigation to include optimum values for all processing parameters. Moreover, a recently proposed modification to improve the films conductivity value is studied more profoundly [29]. The modification is based on altering the hydrolysis reaction in the coating sol through adjusting the water content. The study contributes to deposition of AZO thin films with higher FoM values and therefore, superior optoelectrical performance.

2. Materials and Methods

2.1. Sol preparation

Figure 1 shows the sol preparation steps. Zinc acetate dihydrate (ZAD), $Zn(CH_3COO)_2.2(H_2O)$, was first dissolved at room temperature in a round-bottom twin-neck flask containing 2-methoxyethanol (2-Me) as the solvent and monoethanolamine (MEA) as the stabilizer agent. The concentration of ZAD was 0.2 $mol.L^{-1}$ and the molar ratio of MEA to ZAD was [MEA/ZAD] = 2. Then it was heated under reflux for 1 hour at 70 °C to yield a clear and homogeneous solution. A part of the obtained solution was removed and transferred into another flask and kept under stirring at room temperature to serve as the ZnO sol henceforth. For the remaining part, the doping solution which was ethanolic solution of aluminum nitrate nonahydrate, $Al(NO_3)_3.9H_2O$, was added drop by drop. The molar ratio of the dopant, $[Al^{3+}/Zn^{2+}]$, was precisely selected 2%. Then it was left under reflux for a further 1 hour at 70 °C to get a clear and quite pale yellowish solution. A part of the newly obtained solution was removed once again and transferred into another flask and kept under stirring at room temperature to serve as the pure AZO sol thereafter. The third part of the solution was modified via altering the hydrolysis reaction, through adding drop by drop a precise amount of ultrapure distilled water. The molar ratio of additional water to ZAD was $[H_2O/ZAD] = 2$. Then it was left under reflux for a further 1 hour at 70 °C, whereby a slightly stronger yellowish solution was obtained. It was kept under stirring at room temperature to serve as the modified AZO sol in future. All 3 flasks were dynamically aged for 72 h to yield a proper viscosity and a suitable colloidal condition. A pH measurement was performed for the sols afterwards.

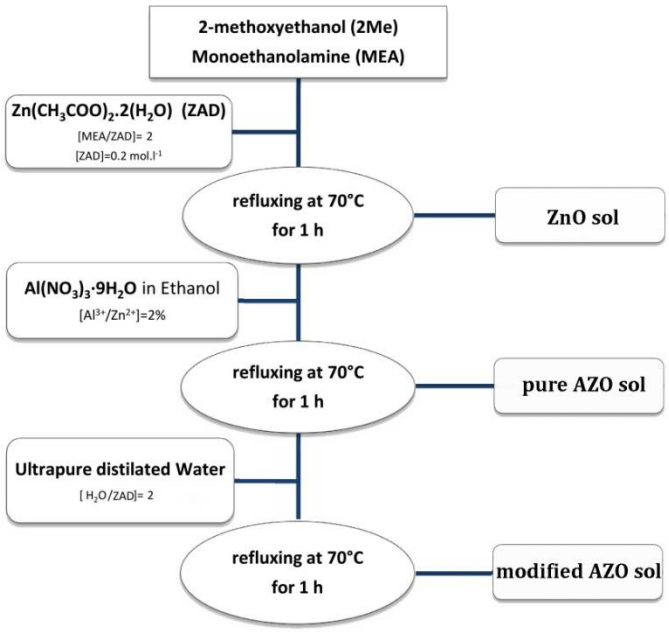

Figure 1. The flowchart summarizing the sols preparation steps.

2.2. Gel and powder processing

The remaining part of the main flask was used to prepare AZO gel and powder. The gel was obtained by keeping a portion of the solution in 80 °C for almost two weeks insofar as that a bright brownish sticky soft substance was obtained. The remaining sol was kept under reflux at 70 °C for 24 hours; whereby white AZO powder precipitated. The powder was collected after three times washing by ethanol and centrifuging, followed by annealing at 600 °C for 2 hours.

2.3. Substrates preparation

The specimens were produced in 2 different groups, the Group A over soda-lime and the Group B over silica substrates, all with the dimension of 1.5*1 in^2. The substrates preparation started by washing them by soap and 5 minutes of ultrasonic cleaning in acetone, ethanol and distilled water respectively. Next, in order to have highly hydrophilic surfaces with outstanding wettability, a ternary treating procedure performed, which was 10 minutes rinsing in piranha solution, then in a 5% solution of ammonium hydroxide and finally in a 5% solution of hydrochloric acid, followed by rinsing in distilled water and drying with compressed nitrogen blow.

2.4. Film deposition and annealing

A home-made dip coating apparatus was used for the film deposition. All depositions were performed under identical condition with a withdrawal speed of 2.5 $cm \cdot min^{-1}$. The dipping chamber was kept at room temperature and filled with N_2 to have a dry atmosphere during the depositions and the subsequent drying. Before dipping the substrates, the coating sols were filtered through Millipore Millex-FG hydrophobic Teflon filters of 0.2 μm. Then they were warmed up to roughly 40 °C in order to insure having a homogeneous viscosity, better substrates coverage and in particular, an enhanced solvent evaporation after the withdrawal. The latter improves the layer thickness uniformity and therefore, avoids formation of pale whitish haze-looking zones on the coated areas [30]. After the withdrawal, samples were kept for 2 minutes in the dry atmosphere of the dipping chamber to start the drying and gelation reaction. It was followed by a 5 minute intermediate heat-treatment through introducing the Group A and Group B samples to an electrical furnace heated up to 275 °C and 430 °C respectively. The layer deposition cycle was repeated 15 times for each sample to obtain an adequate thickness. At the end, the final heat-treatment was performed in static air for 1 hour at 500 °C and 600 °C for Group A and Group B respectively. An additional heat-treatment was also performed only for Group B samples in Ar flow at 600 °C for 1 hour followed by another 1 hour at 400 °C in Ar/H_2 flow containing 3% hydrogen. The thermal treatment details and thermal history of samples is summarized in Table 1.

Table 1. The thermal treatment details and thermal history of samples.

Samples (Substrate)	**Intermediate heat-treatment**	**Final heat-treatment**	**Additional heat-treatment**		
Group A (Soda lime)	static air at 275 °C for 5 minute	static air at 500 °C for 1 hour	none		
Group B (Quartz)	static air at 430 °C for 5 minute	static air at 600 °C for 1 hour	Ar flow at 600 °C for 1 hour	Ar/H_2 flow at 400°C for 1 hour	cooled down to RT* in Ar/H_2 flow

*room temperature

2.5. Characterization

DTA-TG measurements were performed on a Netzsch STA-409 instrument, in the range of 20–700 °C with a heating rate of 10 $°C.min^{-1}$, in static air; alumina crucibles for both reference and sample were used. Baseline correction for DTA curve and buoyancy correction for TG were carried out by means an empty crucibles experiment. FT-IR analysis was performed with a Nicolet Avatar 330 instrument, in transmittance mode; powdered gel was dissolved in KBr in order to get a pellet. The same instrument was further utilized to measure the IR transmittance of the deposited thin films as well. Usual adopted scan conditions were; 4000-400 cm^{-1} as the wavenumber range; number of scans equal to 64 with a resolution of 4 cm^{-1}. XRD spectra were acquired on a RigakuDMax-III D diffractometer, employing a CuKα radiation (λ=0.154056 nm) and a graphite monochromator in the diffracted beam. Asymmetric scattering configuration was adopted for film measurements, with

typical parameter values: scan range in 2θ: 10°-50°; counting time: 10 s; sample interval: 0.1°; incidence angle set at 1°. For the evaluation of crystallite dimensions, line profile analysis on the fitted peaks was performed with MAUD software [31]. To measure the sheet resistance of the obtained films in square geometry, the four-point probe method was applied at room temperature. The films thicknesses were determined through spectroscopic ellipsometry by a HORIBA-UVISEL ellipsometer equipped with DeltaPsi2 software. Finally, the normal transmittance and near-normal reflectance spectra were obtained by UV-Vis-NIR spectrophotometer JASCO V570 at room temperature in the range of 300–2500 nm with the resolution of 2 nm.

3. Results

Figure 2 shows TG-DTA and derivative curves of the dried AZO gel heated in static air with the rate of 10 °C.min^{-1}. It indicates that the weight loss occurs in two different steps. The first one is observed as a sharp drop down to nearly 55% in the range of 195 to 275 °C, corresponding to the endothermic peak centered at 250 °C. During the other step, a mild weight loss starts at around 275 °C and continuous in a long temperature range up to 590 °C, comprising about other 15% weight loss. In the DTA graph, it associates with a long-range exothermic pattern resulting from successive exothermic reactions overlap, from which the sharp ones centered at around 300 °C and 485 °C are identified. No other weight loss is observed after 600 °C.

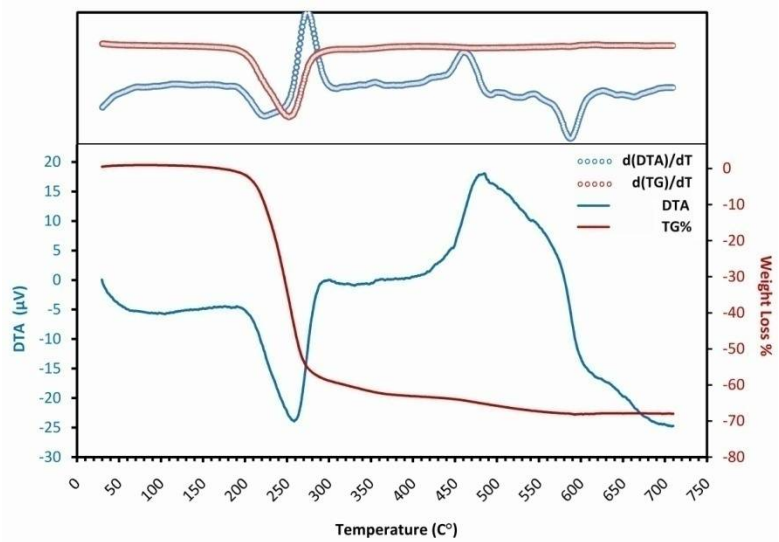

Figure 2. The TG-DTA graph of the dried gel. The derivatives are plotted in the upper part.

Figure 3 illustrates IR spectra of the dried AZO gel and its thermal evolution at 275 °C, 430 °C and 600 °C, in addition to ZAD, MEA and 2-ME data as the initial compounds. Higher magnifications of the graph are also included from the spectral range of 400-700 cm^{-1}, 1200-1800 cm^{-1} and 2500-3200 cm^{-1} corresponding to the IR spectrum range of Zn-O, carboxyl COO and amine CH_2 bonds respectively.

Preprints (www.preprints.org) | NOT PEER-REVIEWED | Posted: 5 May 2019 doi:10.20944/preprints201905.0022.v1

Peer-reviewed version available at Materials 2019, 12, 1744; doi:10.3390/ma12111744

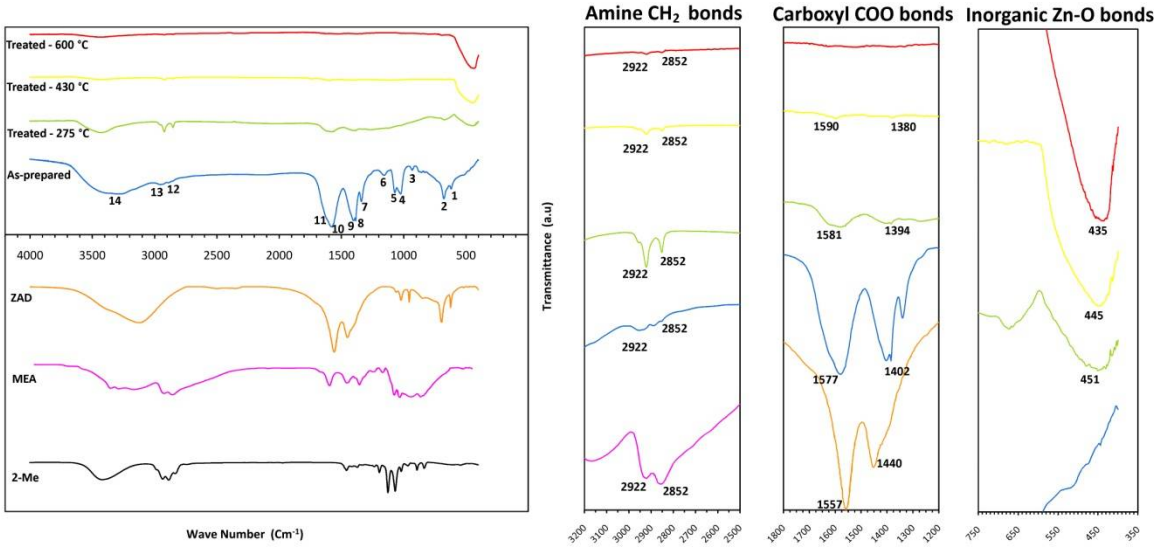

Figure 3. The IR spectra of the as-prepared AZO gel and its thermal evolution at 275°C, 430°C and 600 °C (Upper left), in addition to the data of initial compounds, ZAD, MEA and 2-ME (Lower left). Magnified parts of the spectra regarding CH_2 bond, COO bond and Zn-O bond (Right). The initial compounds data were taken from Bio-Rad's IR spectral databases.

For the dried gel, a superposition of ZAD and MEA peaks is observed, mainly including CH_3, COO and OH absorption peaks of ZAD in the range of 1000-1100 cm^{-1}, 1400-1600 cm^{-1} and 3200-3400 cm^{-1} respectively; as well as CH_2 deformations and CH_2 stretching peaks of MEA in the range of 1300-1500 cm^{-1} and 2800-3000 cm^{-1} respectively. The 2-Me peaks must be overlapped by other peaks since the long-term evaporation allows just a little amount of 2-Me remains in the sticky gel. Distinct absorption peaks of the as-prepared gel are numbered as 1 to 14 under the spectrum and their wavenumbers as well as brief explanations regarding the bonds and vibration modes of the constituent peaks are listed in Table 2.

Table 2. Wavenumbers of distinct absorption peaks in the IR spectrum of as-prepared gel, numbered as 1 to 14 in Figure 3. The molecular bonds and vibration modes of the constituent peaks are provided.

Observed peak (cm^{-1})		Assignments	Observed peak (cm^{-1})		Assignments
1	**622**	π (COO) ⟶ ZAD	9	**1402***	symmetric stretching (COO) ⟶ ZAD scissor deformation (CH_2) ⟶ MEA
2	**696**	α (COO) ⟶ ZAD	10	**1577**	asymmetric stretching (COO) ⟶ ZAD
3	**941**	out-of-plane deformation (NH_2) ⟶ MEA	11	**1593***	in-plane deformation (NH_2) ⟶ MEA
4	**1024***	rocking (CH_3) ⟶ ZAD stretching (CO) ⟶ MEA	12	**2852**	symmetric stretching (CH_2) ⟶ MEA
5	**1072***	rocking (CH_3) ⟶ ZAD stretching (CN) ⟶ MEA	13	**2922**	asymmetric stretching (CH_2) ⟶ MEA
6	**1150**	stretching (COH) ⟶ MEA	14	**3000-3500***	asymmetric stretching (OH) ⟶ MEA asymmetric stretching (OH) ⟶ ZAD asymmetric stretching (NH_2) ⟶ MEA symmetric stretching (NH_2) ⟶ MEA
7	**1342**	symmetric bending (CH_3) ⟶ MEA			
8	**1384**	symmetric bending (CH_2) ⟶ ZAD symmetric bending (CH_3) ⟶ ZAD			

* Overlap of two or more peaks

While no evidence is detected for Zn-O bond in the gel, after heat-treatment at 275 °C, together with a considerable reduction of all organic bonds, an absorption peak of metal oxide bond appears at around 451 cm^{-1}. It is related to the stretching vibration of Zn-O bond in tetrahedral coordination [32]; whereas we cannot clearly conclude about the presence of Zn-O bond in octahedral

Peer-reviewed version available at Materials 2019, 12, 1744; doi:10.3390/ma12111744

coordination that shows absorption peak at around 670 cm^{-1} [32], due to overlapping with α and π bonds of COO peaks of ZAD. The trend continues for the treated gels at 430 and 600 °C with increasing the peak intensity of Zn-O bond in tetrahedral coordination and diminishing of remaining organic bonds, while the formation of Zn-O bond in octahedral coordination seems to be totally insignificant. In the spectra of treated gel at 600 °C just a sharp Zn-O bond peak is detected with a minor trace of CH_2 and OH bonds.

In Figure 4, the XRD patterns concerning the samples of both groups after the final heat-treatment are displayed in addition to the spectrum of the calcined powder. By performing the curve fitting on the peaks through the MAUD software, the thin films microstructural parameters, shown in the Table 3, were evaluated. The texture coefficient of (002) peak, $T_c(002)$, was also calculated for each sample, using the equation (3), in order to quantify the structural mono-orientation toward this plane;

$$T_c(002) = \frac{[I(002)/I_p(002)]}{\frac{1}{n}.\sum[I(hkl)/I_p(hkl)]}, \quad (3)$$

where $I(hkl)/I_P(hkl)$ denotes the ratio of (hkl) peak intensity in the textured sample to the one in the randomly oriented pattern (powder); n is the number of considered reflections; and $\Sigma[I(hkl)/I_P(hkl)]$ indicates the summation of ratios for all n reflections [33]. The texture coefficient of planes in the powder pattern is $T_c(hkl)=1$; and any deviation in thin films patterns as $T_c(hkl) > 1$ or $T_c(hkl) < 1$ implies a preferred growth, as abundance or scarcity of grains oriented in the related direction respectively [34]. Moreover, the relative intensity of (002) peak, $I_r(002)$, was calculated as the ratio of the (002) peak intensity to the summation of all reflections intensities [35].

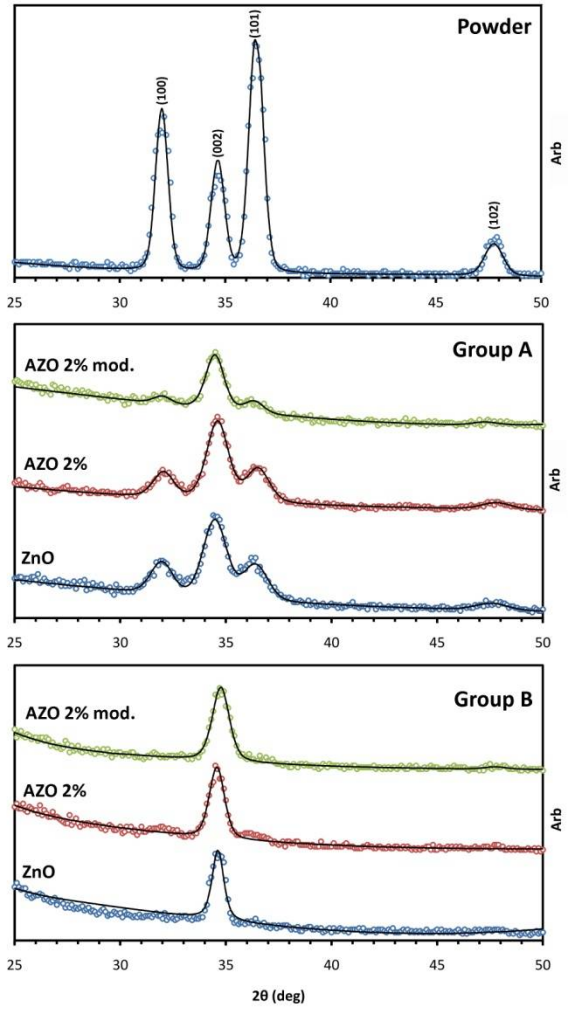

Figure 4. X-ray diffraction patterns for the powder particles and Group A and B samples after the final heat-treatment.

Table 3. The results of line profile analysis on of the fitted peaks of thin films illustrated in Figure 4.

Samples		Crystallite Size (nm)	c-axis Microstrain (%)	Texture	
				$T_c(002)$	$I_r(002)$
Group A	**ZnO**	27±2	-0.12	2.25	0.56
	AZO2%	20±1	-0.29	2.34	0.58
	AZO2% mod.	22±2	-0.23	2.94	0.73
Group B	**ZnO**	29±2	-0.11	3.92	0.98
	AZO2%	24±1	-0.25	3.84	0.95
	AZO2% mod.	27±1	-0.19	3.98	0.99

For the evaluation of electrical properties, 4-point probe test was performed on samples after the final and additional heat-treatments. The results in the form of sheet resistance, R_{sh}, and resistivity, ρ, are reported in Table 4. R_{sh} values, averaged on four different measurements, were estimated using the equation (4) as

$$R_{sh} = \left(\frac{\pi}{\ln 2}\right)\frac{\Delta V}{I}, \quad (4)$$

in which ΔV is the potential difference between the voltage probes while the constant current flow of I is induced to the sample via the current probes. The ratio is multiplied by correction factor for thin films [36]. Then, ρ values were obtained by multiplying R_{sh} to the film thickness value which was determined as d = 106±2 nm. The degree of uncertainty is difficult to quantify, but the deviation was considered mainly due to systematic errors resulting from probes surface area and their non-ohmic contacts, which affects the relative behavior of different films in a similar way [37].

Table 4. The results of 4-point probe test on sheet resistance and resistivity values.

Samples		After final heat-treatment		After additional heat-treatment	
		R_{sh} (Ω/sq)	ρ (Ω.cm)	R_{sh} (Ω/sq)	ρ (Ω.cm)
Group A	**ZnO**	10^6 <	10 <		
	AZO2%	348.6×10^3	3.7±0.3	-	-
	AZO2% mod.	294.4×10^3	3.2±0.1		
Group B	**ZnO**	10^6 <	10 <	298.5×10^3	3.1±0.2
	AZO2%	49.7×10^3	0.52±0.2	1.3×10^3	$(14.5\pm0.3)\times10^{-3}$
	AZO2% mod.	38.4×10^3	0.41±0.1	543.7	$(5.9\pm0.1)\times10^{-3}$

The optical transmittance T and reflectance R spectra of Group B samples after the additional heat-treatment are compared in Figure 5. An extended spectrum in IR range is included for the transmittance as well. Since the measured values of T and R are affected by the substrate, following equations were used to estimate the films absolute values, supposing that the substrate is homogenous and transparent with negligible absorption [38]:

$$\begin{cases} T = \dfrac{1 + R_0 - 2\Phi_R(R_0)^2}{(1 + R_0)^2 - (R_0.\Phi_T)^2}.\Phi_T \\ \\ R = \dfrac{2(1 + R_0)\Phi_R - (\Phi_T)^2}{(1 + R_0)^2 - (R_0.\Phi_T)^2}.R_0 \end{cases}; \quad (5)$$

in which R_0 is defined by the refractive index of substrate, ns, as $R_0 = \frac{(1-n_s)^2}{(1+n_s)^2}$, and $\Phi_R = \frac{R_{meas}}{R_s}$ and $\Phi_T = \frac{T_{meas}}{T_s}$ represent the ratio of the measured reflectance and transmittance of the sample to the ones of the bare substrate respectively. Having the absolute values of T and R, the absorptance A is

Peer-reviewed version available at Materials 2019, 12, 1744; doi:10.3390/ma12111744

obtained as A% = 100– T%– R%. Average values of spectrophotometry measurement within the visible range from 400 to 700 nm are reported for all samples in Table 5 as $\bar{T}$% , $\bar{R}$% and $\bar{A}$%.

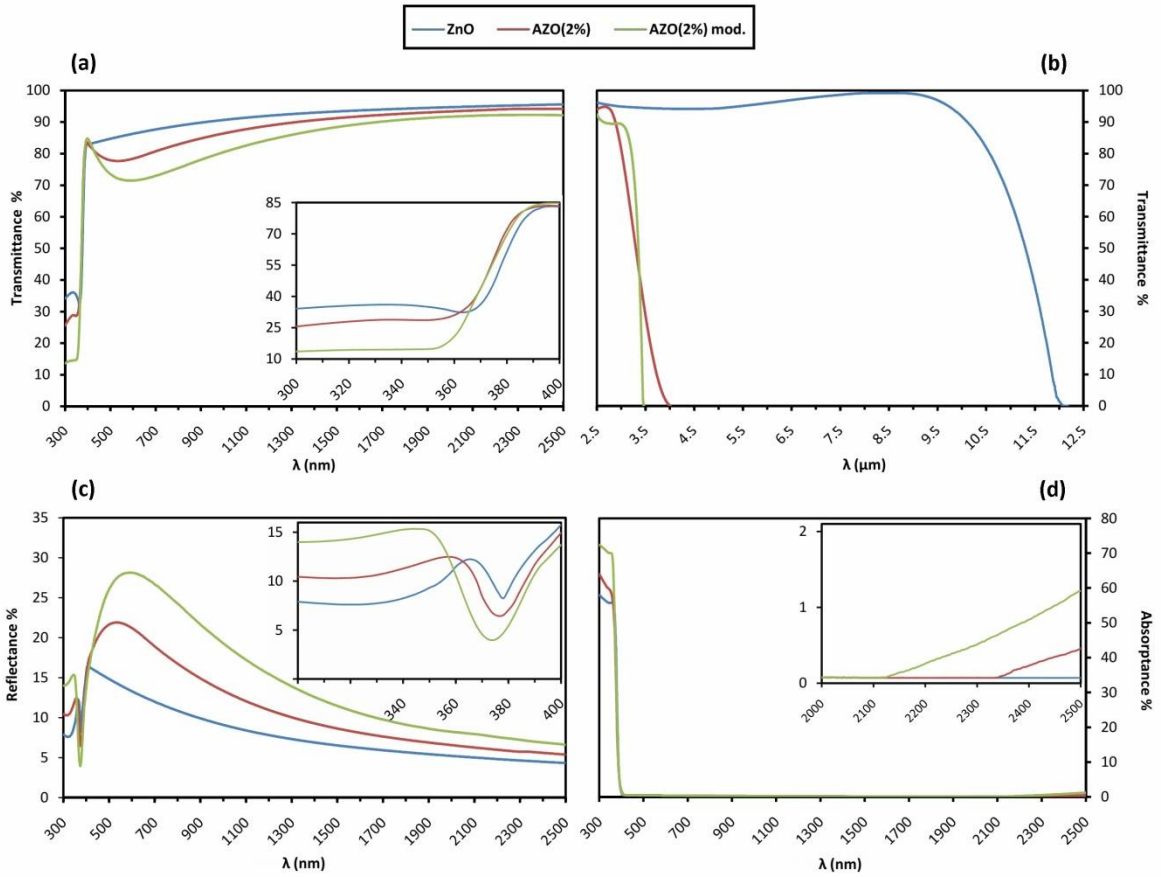

Figure 5. UV-Vis-NIR spectra of Group B samples; (a) transmittance (b) extended transmittance (c) reflectance and (d) absorptance. Inset graphs for (a) and (b) show the magnification around the absorption edge while for the absorptance spectra the inset is the magnification of the far right range.

The absorption coefficient α as a function of T and R values and the film thickness d is given by the following equation which takes into account the multiple internal reflections [39]:

$$\alpha = \frac{1}{d}\ln\left[\frac{(1-R^2)}{2T} + \sqrt{\frac{1-R}{4T^2} + R^2}\right]. \quad (6)$$

Having α, the optical band-gap energy E_g was estimated from the conventional Tauc-plot method. According to Tauc empirical rule [40], for the incident photons with energy levels higher than E_g which are identified by the fundamental absorption; α is a function of photon energy $E = h.\nu$ with the below equation for the direct transition occurring in ZnO band structure:

$$\alpha.h\nu \sim (h\nu - E_g)^{0.5}; \quad (7)$$

so the extrapolation of the linear part of $(\alpha.h\nu)^2$ versus $h\nu$ gives the approximate E_g value at the $h\nu$ axis; as illustrated in Figure 6(b). However, this equation assumes an ideal parabolic band structure and it is reported that in case of broadening of the fundamental absorption edge as a result of doping or structural non-uniformities, Tauc-plot method may underestimate E_g [43,45]. Therefore, a corrected value of E_g was determined by an alternative method using the maximum of the first derivative of absorption coefficient as the function of photon energy, $d\alpha/d(h\nu)$ [44-46], as shown by dotted lines in Figure 6(c). All curves follow the Gaussian trend depicted with solid fitting lines. The difference between the obtained values for the band-gap energy ΔE_g is associated with the degree of absorption edge broadening and is shown to be related to the damping energy Γ by $\Delta E_g = (\pi/4)\Gamma$ [40]. The E_g values calculated by both methods in addition to Γ values are reported in Table 5.

For the incident photons with the energy just below the band-gap energy, α shows another form of dependency on hν as stated by Urbach empirical rule [44]:

$$\alpha \sim \exp\left(h\nu / E_u\right); \quad (8)$$

in which E_u is the Urbach energy, corresponding to the width of the absorption edge below the band-gap [45]. By plotting Ln(α) versus hν, the value of E_u is calculated by taking the reciprocal of the slope of the linear part in the lower photon energy region of the curve, as depicted in the inset of Figure 7(b). The obtained values of E_u are reported in Table 5.

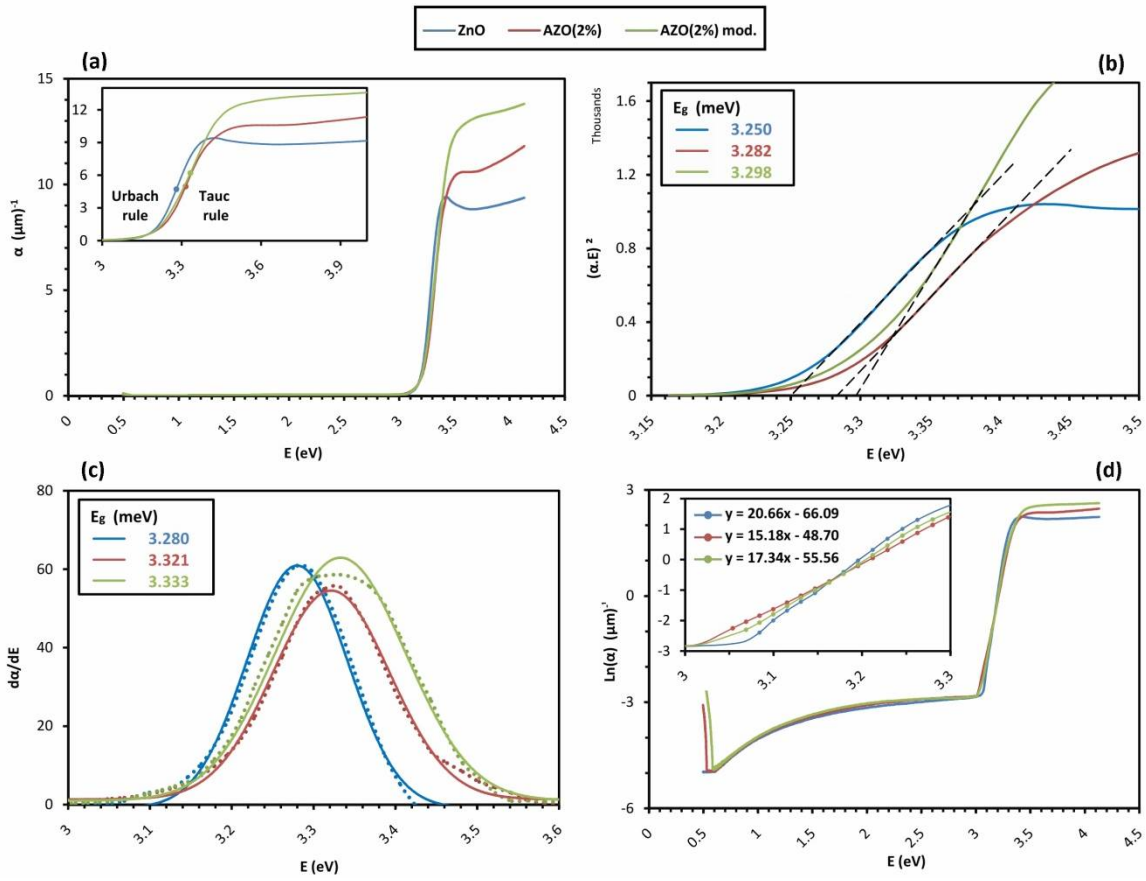

Figure 6. (a) The plot of α (μm^{-1}) versus hν. The inset is the magnification of the high energy part and shows the regions governed by Tauc and Urbach rules. The band-gap energies are marked with solid dots. (b) Determination of the band-gap energies via the Tauc-plot method; and (c) the alternative method to find the band-gap using the maximum of the dα/d(hν) curve (dotted curves). The solid curves show the Gaussian fits for dα/d(hν) curves. (d) The plot of Ln(α) (μm^{-1}) versus hν. The inset shows the magnification of the linear parts. The slopes indicate E_u values reciprocally.

Finally, the optical parameters were calculated including the refraction function as $\bar{n} = n + i\kappa$ and the relative permittivity function as $\bar{\varepsilon} = \varepsilon + i\acute{\varepsilon}$; where the absorption index κ, refractive index n, and real and imaginary parts of relative permittivity, ε and $\acute{\varepsilon}$ were obtained via the relations below:

$$\begin{cases} \kappa = \alpha\lambda/4\pi & R = \dfrac{(n-1)^2 + \kappa^2}{(n+1)^2 + \kappa^2} \\ \varepsilon = n^2 - \kappa^2 & \acute{\varepsilon} = 2n\kappa \end{cases}. \quad (9)$$

Then, n values as a function of λ was fitted to Cauchy dispersion formula [46]. The result is illustrated in Figure 7. The n values at λ = 450 nm were used to estimate the porosity p of films through Lorentz–Lorentz equation [50-52]:

$$p = 1 - \frac{(n^2-1)/(n^2+2)}{(n_B^2-1)/(n_B^2+2)}; \quad (10)$$

Preprints (www.preprints.org) | NOT PEER-REVIEWED | Posted: 5 May 2019 doi:10.20944/preprints201905.0022.v1

Peer-reviewed version available at Materials 2019, 12, 1744; doi:10.3390/ma12111744

considering that n and n_B are refractive index values of the film and of the pure ZnO bulk respectively. The estimated values for n and p% are listed in Table 5.

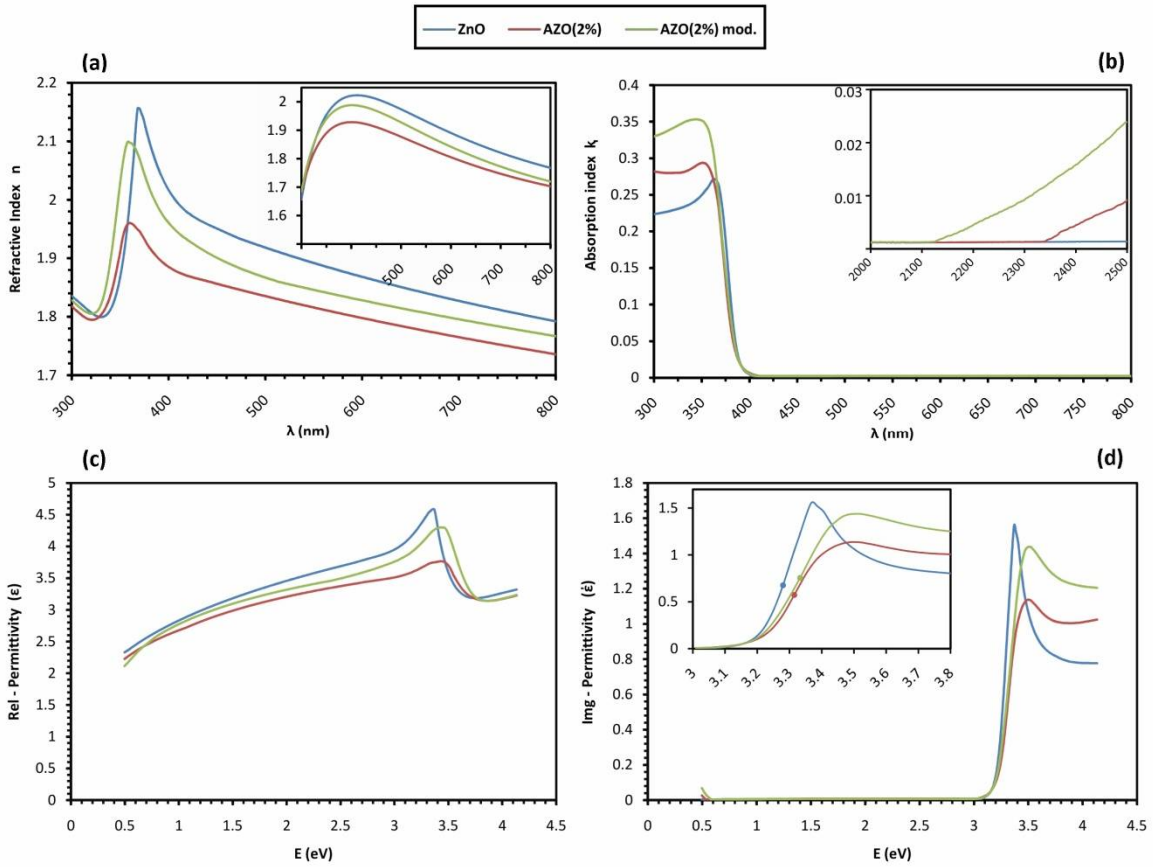

Figure 7. Calculated optical parameters of the films; (a) and (b) are the refractive index n and the absorption index k as functions of wavelength respectively. The inset shows n values fitted to Cauchy dispersion formula. (c) and (d) are the real part and imaginary part of relative permittivity, ε and ε̇, as functions of photon energy respectively. The inset shows the magnified part of ε̇ around the absorption edge and the band-gap energies are marked out with solid dots.

Table 5. A summary of observed values for the optical properties of Group B samples after the additional heat-treatment.

Samples		Spectrophotometry $\bar{T}$(%)	$\bar{R}$(%)	$\bar{A}$(%)	Band-Gap E_g (eV) Tauc-plot	dα/d(hν)	Urbach Energy E_u (meV)	Damping Energy Γ (meV)	Refractive Index* n	Porosity** p(%)
Group B	**ZnO**	87.7	11.8	0.4	3.25	3.28	48.4	38	2.01	6.4
	AZO2%	82.3	17.1	0.5	3.28	3.32	65.8	49	1.96	16.2
	AZO2% mod.	79.1	20.3	0.5	3.29	3.33	57.6	44	1.92	13.5

*at λ = 450 nm from the fitted graph. **considering $n_B = 2.12$ [49].

By the data reported in Tables 4 and 5 about R_{sh} and $\bar{T}$ values and using the Equations (1) and (2), the FoM values of the Group B samples after the additional heat-treatment films were obtained as displayed in Table 6.

Table 6. Calculated FoM values for Group B samples after the additional heat-treatment through 3 different equations.

Samples		Haacke FoM [4]	Jain-Kulshreshtha FoM [3,5]	Gruner-Coleman FoM [8,9,11]
Group B	**ZnO**	8.61×10^{-7}	2.46×10^{-5}	9×10^{-3}
	AZO2%	1.07×10^{-4}	3.9×10^{-3}	1.4
	AZO2% mod.	1.72×10^{-4}	7.7×10^{-3}	2.75

4. Discussion

The electrical and optical properties of the obtained films are associated with the preferred crystallization orientation and grain-boundary characteristics of their microstructures [17]. These features are correlated with the both 1) sol chemistry, as it determines the nature and amount of the species in the amorphous deposited layer; and 2) thermal treatment procedure, which induces the nucleation and crystal growth as well as the decomposition and the release of organic molecules. Generally, the oriented crystallization toward the c-axis is energetically-preferred in ZnO thin films over the substrate [23]. Based on the Ohyama proposed explanation [23], the preferred orientation toward the c-axis is even enhanced in case of less overlapping and coincidence of steps of this sequence: (a) evaporation of the liquid phase and decomposition of the organic residue, and (b) crystallization of the oxide film. Since the structural relaxation of the gel, as a prerequisite for the oxide film crystallization, originates from the evaporation of the liquid phase and decomposition of the organic residue, the better separation of steps helps avoiding any deterioration of crystallization uniformity. Such a separation is taken into account by performing the first step during intermediate heat-treatments and postponing the second one to the final heat-treatment. It requires knowing physical and chemical properties of the sol species such as boiling temperature and molecular bonding, in addition to the gel reaction to high temperature. So a detailed study on the sol chemical evolution as well as the thermal evolution of the gel is taken into consideration; followed by the consequent effects of different sol chemistry and thermal treatment procedure on the microstructural features. Finally, the different optoelectrical behavior arises from the modified microstructure is compared with those of others and evaluated by FoM value.

4.1. Evolution of the sol

While the commonly used sol–gel routes to synthesize metal oxides are based on hydrolysis reactions of metal-alkoxides or their inorganic salts in organic solvents or aqueous media respectively [51], for ZnO-based compounds, using ZAD as an organic salt in an alcoholic solvent has been reported more often, which is an intermediate between the two conventional sol–gel routes. In such conditions, an in-situ formation of alkoxide- or hydroxide-based compounds happens initially and then they transform into metal oxide nanoparticles via hydrolysis and condensation reactions [52].

The experiment in this study starts by adding 2-ME to the ZAD precursor which results in the formation of zinc monoacetate, Zn(OAc) [53], while the expected zinc alkoxide is inhibited to form; since the solubility of simple zinc alkoxides in alcoholic media is restricted to just long-chain alcohols such as oleyl alcohol [57,58]. Then, the supposedly released water molecules of ZAD start to hydrolyze Zn(OAc), forming zinc hydroxide, $Zn(OH)_2$, which will undergo condensation to form ZnO during the forthcoming thermal treatment. However, due to the low initial amount of water supplied by ZAD, the rate of assumed hydrolysis is low [56]. Addition of water in this step is not helpful and should be avoided; as otherwise, since the solubility of $Zn(OH)_2$ in alcohols is limited, white solid $Zn(OH)_2$ precipitates [57]. Moreover, the limited solubility in alcohols applies to ZAD as well; because the coulombic hydration sheath surrounding a zinc cation remains attached with it inside non-polar solvents and prevents the dissolution [57,61]. Consequently, all reactions develop just very partially, resulting in a turbid grayish solution. Eventually, any hydrolysis through the aqueous route is considerably insignificant.

In order to improve the solubility, it is necessary to introduce an additive compound such as monoethanolamine (MEA) that acts as a nucleophilic agent towards Zn ions. MEA has two Lewis base groups, a hydroxy and an amine and it is capable of making a bidentate ligand, whether as a chelate to one ion or a bridge between two Zn ions [59]; however, a chelating ligand is expected to be more stable [63,64]. In a similar way, in ZAD and Zn(OAc), acetate is a Lewis base and a chelating ligand exists between the acetate oxygen atoms and Zn ion; while water molecules form a hydration sheath around the metal core [65,66]. It is reported that by adding amine-containing compounds, the hydration sheath is disturbed and water molecules are released [58]. Moreover, instead of a selective coordination and ligand exchange with the acetate anion, an additional coordination happens [64].

Preprints (www.preprints.org) | NOT PEER-REVIEWED | Posted: 5 May 2019 doi:10.20944/preprints201905.0022.v1

Peer-reviewed version available at Materials 2019, 12, 1744; doi:10.3390/ma12111744

Therefore, the MEA molecule alongside the acetate ion forms a complex ion cooperatively, in which the central metal ion is coordinated by two chelating ligands; a metal-oxygen core formed by the acetate ion, covered by an organic shell made by MEA. The solubility of the new complex compound, referred by [MEA][Zn(OAc)], in the non-polar solvent of 2-ME is much more than before the addition of MEA; so that a clear transparent solution is obtained. However, based on DFT calculations, such a mono-nuclear compound is not thermodynamically stable in the solution and a dimer structure, $[MEA]_2[Zn(OAc)]_2$, has nearly 50 kcal.mol^{-1} free energy less than two monomers [65]. In the solid phase, the most stable compound has a tetramer structure, $[MEA]_4[Zn(OAc)]_4$, formed by the union of two dimers [66]. Figure 8 illustrates the structural formula related to each one.

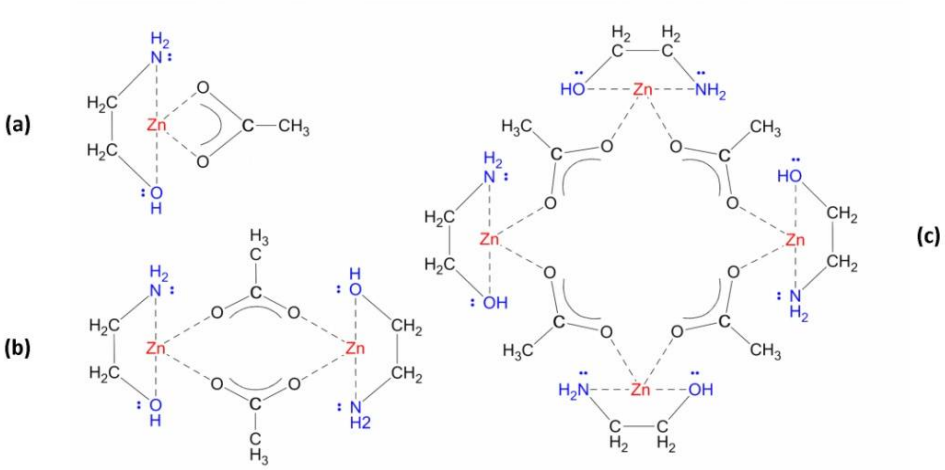

Figure 8. Proposed structural formula of different forms of the complex compound as a, (a) monomer, (b) dimer and (c) tetramer.

As depicted in Figure 8, in the monomer structure, likewise ZAD, there is a chelating ligand between any acetate and Zn ions; while in dimer and tetramer structures, each acetate anion forms a bridge ligand between two metal ions. Similar result regarding the bonding condition was reported through NMR analysis as well [65].

The subsequent transformation of the sol species depends on the competition for the Zn Lewis acid center between nucleophilic species of (-NH_2) and $(CH_3COO)^-$ as the capping agents, and $(OH)^-$ as the hydrolysis agent [59,70]. Considering a fixed amount for acetate anions, it is possible to modify the sol evolution by changing the molar ratio of the other species in so far as the solution remains clear and in equilibrium condition.

The presence of free $(OH)^-$ primarily originates from the basic environment. Owing to $[H_2O/Zn^{2+}] = 2$ in ZAD, the typical initial condition is $[OH^-/Zn^{2+}] = 1$. However, unlike before the addition of MEA, it is possible to manipulate the ratio by adding a limited amount of extra water, inasmuch as the solution remains clear. The experimented molar ratio of $[H_2O/ZAD] = 2$ for additional water increases the amounts of free $(OH)^-$ to $[OH^-/Zn^{2+}] = 2$. It was observed that the addition of more water makes the solution translucent and disturbs the equilibrium. For (-NH_2), the ratio of $[MEA/Zn^{2+}] = 1$ is extensively used in literature; however, several researchers have reported that in case of $[MEA/Zn^{2+}] = 2$ a more enhanced texture orientation toward c-axis direction of zincite structure [59, 23, 71] and also finer crystallite size with less porosity is obtained [69]. This approach is also confirmed by the investigations exclusively devoted to study the effect of amino-additives amount on the microstructural features of ZnO thin film [24,25,72,73]. While an equimolar ratio of $[MEA/Zn^{2+}]$ is enough to form the [MEA][Zn(OAc)] spices, a higher ratio increases the solution pH value, which affects the formation of ionic zinc complexes. It is known that the stable ionic form of Zn in the solution varies by changing the pH; from Zn^{2+} in acidic conditions to non-ionic state when 6

< pH < 8, and to Zn^{2-} in highly basic condition of pH > 12 [73]. The latter pH value, which can facilitate formation of a stable hydroxide-based complex ion, was obtained by [MEA/Zn^{2+}] = 2 in the present study.

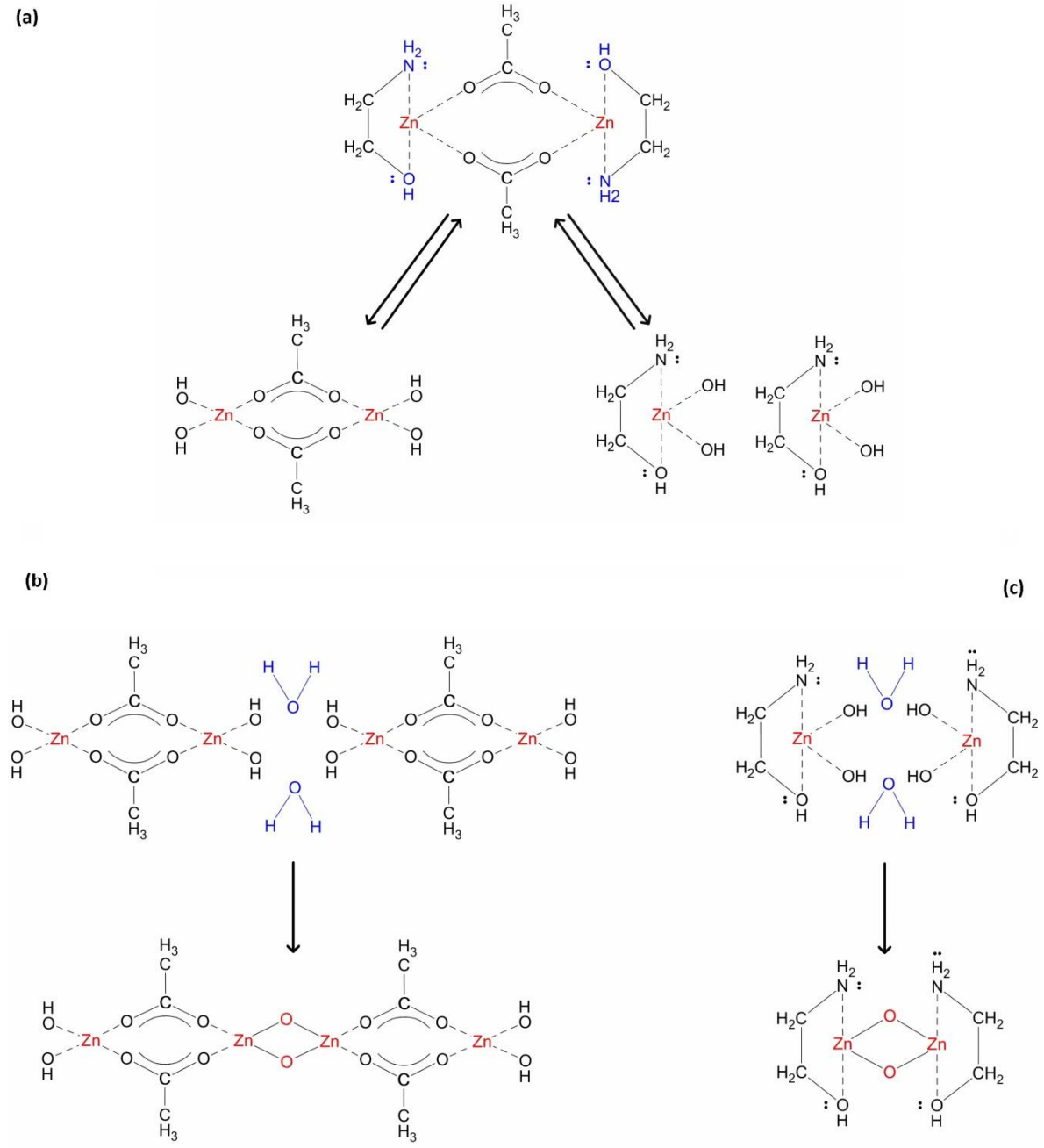

Figure 9. Suggested mechanism for possible hydrolysis (a); and condensation reactions (b) and (c).

Considering the condition obtained from the applied ratios of [OH^-/Zn^{2+}] and [MEA/Zn^{2+}], following the addition of extra water, the hydrolysis reaction accelerates and continues throughout the reflux time. It originates from attacking the highly nucleophilic $(OH)^-$ to the core of the complex, transforming it to a hydroxide-based complex as depicted in Figure 9(a).

During the aging time, the hydrolysis products are in equilibrium with the initial complex but they may engage in condensation reaction if water molecules are present, illustrated by Figures 9(b)

and 9(c). It involves linking of the hydrolysis products through formation of metal-oxygen bonds in an oxolation condensation.

4.2. The gel thermal evolution

Transformation of the gel layer into the oxide film is a multiple-step process. It involves formation of metastable intermediates, pyrolysis and decomposition of organic parts, initiation and development of a network of metal oxide crystallites by nucleation and growth mechanisms as well as releasing the residuals outwards. The initial part of such a process occurs during the drying and intermediate heat-treatment which is performed between each layer deposition; while the rest happens throughout the final heat-treatment within the whole of the layers collectively. The extent to which the transformation develops during the intermediate heat-treatments is decisive in the crystallization behavior and the microstructure of the final film [72].

In the gel IR spectrum, in spite of overlapping, it is clear that absorption peaks (listed in Table 2) follow a simple superposition of MEA and ZAD peaks. As a suitable indication, we can follow the stretching COO peaks of ZAD (the peaks numbered as 9 and 10) and the stretching CH_2 peaks of MEA (those numbered as 12 and 13) due to their higher intensities in the initial compounds and being relatively less influenced by overlapping. It is observed that while CH_2 peaks of MEA appear without any shifting in the IR spectrum of the gel, the two stretching COO peaks of ZAD, referred by $\nu_{symmetric}$ and $\nu_{asymmetric}$, show a diverging shift in their wavenumbers. In other words, if the wavenumber separation value is defined as $\Delta\nu = (\nu_{asymmetric} - \nu_{symmetric})$, for stretching COO peaks we have: $\Delta\nu_{(ZAD)} < \Delta\nu_{(gel)}$, as it is clear in the magnified part of Figure 3 in the carboxyl COO bonds frame. It is reported that $\Delta\nu$ value is the characteristic of acetate/metal bonding form and as a general rule: $\Delta\nu_{(chelating)} < \Delta\nu_{(bridging\ bidentate)} \leq \Delta\nu_{(ionic)} < \Delta\nu_{(unidentate)}$ [66,75,76]. Accordingly, while in the ZAD structure nearly all bonds between acetate groups and Zn ion are chelating ligands, bridging bonds are expected to exist in the gel. It is in accordance with the presence of thermodynamically more stable dimers and tetramers of [MEA][Zn(OAc)] with bridging ligands instead of monomers with chelating ligands.

In the IR spectrum of the treated gel at 275 °C, the most noticeable feature is a drastic decrease in absorption peaks of organic bonds. It shows that the 55% weight loss and the endothermic peak observed in 195-275 °C of TG-DTA graph are related to decomposition of zinc-organic compounds. Comparing with the spectrum of the as-prepared gel, the intensity reduction is more evident for the stretching COO peaks of ZAD than the stretching CH_2 peaks of MEA. (In the gel spectrum, a considerable part of CH_2 peaks is hidden due to overlapping with the broad OH peak of ZAD). So it can point to the fact that compounds containing acetate group experienced more deterioration by 275 °C. Besides, while the $\Delta\nu$ value for stretching CH_2 peaks of MEA remains unchanged, it continues the increasing trend for COO peaks, probably as a result of unidentate bonds formation in decomposed species. The second important feature is the appearance of Zn-O bond absorption peak which indicates the existence of crystalline ZnO with tetrahedral coordination. It means that the exothermic process started at around 250 °C and centered at nearly 300 °C could be associated to the AZO crystallization from newly-decomposed zinc compounds. Eventually, 275 °C was selected as the lower limit for intermediate heat-treatment temperature, since it separates the first sequence of decomposition-crystallization.

At 430 °C, the TG analysis shows 10% weight loss more than that of observed at 275 °C; and it is correlated with the ongoing reduction in the intensity of organic bonds peaks in the IR spectrum. Since the maximum weight loss obtained through TG analysis is around 70%, a great amount of organic compounds are decomposed by 430 °C, including those containing MEA. Furthermore, the relatively sharper Zn-O bond absorption peak indicates a fair development in AZO crystallization during 300-430 °C. However, the DTA graph does not show the features regarding neither an ongoing decomposition nor a crystallization development. Instead, an almost flat line with a subtle positive sloop is observed which may originates from overlapping of two different peaks happening simultaneously in 300-430 °C; an endothermic peak related to decomposition of organic species containing MEA and an exothermic peak associated to AZO crystallization. Following 430 °C, a net

exothermic peak shows that the crystallization overcomes the decomposition afterwards. Accordingly, 430 °C was selected as the higher limit for intermediate heat-treatment temperature since it separates the second sequence of decomposition-crystallization.

The IR spectrum of 600 °C shows a very sharp peak of Zn-O bond in tetrahedral coordination in an organic-free background; nevertheless, an extremely weak yet-detectable pair of peaks related to CH_2 bond of MEA is present. This temperature is associated with 70% weight loss in the TG graph which remains constant up to the end of analysis at 700 °C. So for the final heat-treatment temperature, 600 °C is a suitable choice.

4.3. Structural analysis of the films

X-ray diffraction patterns in Figure 4 together with the extracted data in Table 3 provide a basis for studying correlation of samples microstructure with the sol chemistry and applied thermal treatment through comparing them with the same batch or with the other group samples. Accordingly, different thermal treatment for Group A and B samples seems to have a determining effect on the texture coefficient T_c and relative intensity I_r of (002) peak; however, other parameters including the crystallite size and lattice strain are less affected by the thermal treatment. The only other noticeable variation is observed in comparing AZO structures with the undoped ZnO ones; where altering the sol chemistry by the introduction of Al^{3+} dopants causes smaller crystallite sizes and increased microstrain values, independently of the applied thermal treatment. This is in accordance with observing slight broadening of (002) peaks in AZO patterns. On the other hand, altering the sol chemistry in terms of sol modification seems to have no effect, although the c-axis microstrain values are fairly affected in the modified AZO ones.

In order to discuss about the samples texture, the powder pattern is considered as the reference. This pattern shows a set of well-defined diffraction peaks concerning a highly crystalline phase in the hexagonal zincite structure with randomly-oriented crystallites. For the films of Group A, apart from a lower degree of crystallinity which originates from the small thickness of the films, a great increment is observed for $T_c(002)$ and $I_r(002)$ values, showing a preferred orientation along c-axis. However, only Group B samples display a totally mono-oriented structure along the c-axis direction; whereas the intensity of other peaks is insignificant. At the same time, through comparing the texture values within the groups, it is observed that different chemistry of the deposited sol does not lead to a significant texture variation. So it can be concluded that the structural orientation in the post-annealed films is essentially the matter of nucleation and grain growth [76], depending on the thermal treatment procedure. Accordingly, the thermal treatment with high temperature approach performed on Group B samples at 430 and 600 °C is recognized more appropriate to decrease the overlapping of decomposition and crystallization and therefore, to obtain a structure with stronger c-axis preferred orientation. This conclusion could associate with the TG-DTA measurement result. As mentioned in Section 4.2, the total weight loss of the gel equals to nearly 70%. At 275 °C and 430 °C, the weight loss is roughly 55% and 65% respectively. Thus, performing the intermediate heat-treatment at 430 °C compared with 275 °C remains fewer amounts of organic residual to be decomposed during the final heat-treatment in which, the grain crystallization and growth occur. Consequently, due to less overlapping of crystallization and decomposition, the morphological order of grains follows the energetically-preferred columnar orientation during the nucleation and growth [23] and it is not disturbed with the release of organic residuals. In the nucleation step, the driving force is the reduction of free energy through transformation of the metastable amorphous phase to the crystalline state; so the initial orientation of nuclei develops in a way to bring about the minimum free energy configuration. Considering a heterogeneous nucleation at the film/substrate or film/film interface, since the basal plane in ZnO structure has a lower surface energy [77], the nuclei with their basal plane parallel to the substrate surface possess the smallest free energy. It can be considered as the origin of preferred orientation along the c-axis [76] that is maintained during the crystal growth as well. In the hexagonal structure of ZnO, the two basal planes are composed of just O^{2-} or just Zn^{2+} ions and therefore, due to being polar and metastable, they show a greater reactivity tendency to impose less energy to the system, which results in a faster growth rate. On the

Peer-reviewed version available at Materials 2019, 12, 1744; doi:10.3390/ma12111744

contrary, the lateral planes are non-polar and electrically neutral with a higher stability. Supposing a full coverage of the substrate, in the initially formed particles the c axis-oriented growth perpendicular to the substrate dominates, due to the faster development of the polar planes [56] and a dense columnar morphology is resulted. However, this reasoning is justified when the nucleation occurs mainly at the film/substrate or film/film interface in a heterogeneous manner. If the deposited layer thickness is larger than the average crystallite size, in addition to the heterogeneous nucleation at the interface, the homogeneous nucleation also occurs inside the film volume, resulting in a porous granular morphology [79,80]. In this study, the obtained final thickness after deposition of 15 layers is in the range of 106 ± 2 nm, indicating that the thickness of each individual layer could be estimated to be less than 10 nm. Since this value is considerably smaller than the average grain size of 20 to 30 nm reported in Table 3, a fully-heterogeneous nucleation is claimed in deposition of all layers for the samples of both groups. Therefore, the difference observed in Group A and B samples regarding the $T_c(002)$ and $I_r(002)$ values could be considered as the consequence of the overlapping of decomposition and crystallization.

Regarding the c-axis microstrain values, it is observed that the modified AZO structures in both groups show slightly higher values in comparison with pure AZO ones, considering that the negative sign just indicates the compressive stress mode. Originally, the film stress comprises two components; an intrinsic part due to point-defects and crystal lattice distortions; and an extrinsic part due to the thermal strain related to the different thermal expansion coefficients for the film and the substrate [80]. The latter seems to be insignificant in the c-axis direction; since by assuming the validity of the thin film approximation in having much larger lateral dimensions than that of the thickness, the thermal strain of the film is under a plane stress condition [81]. The intrinsic part mainly results from the substitution of Zn^{2+} by the smaller Al^{3+} ion and/or the presence of oxygen ion vacancies and therefore, it leads to the unit cell contraction and observing compressive strain. For the undoped ZnO samples, the absence of the dopants could lead to lower unit cell contraction and less compressive strain. For AZO samples, the subtle difference in strain values is likely to be caused just by the growth process itself, since the doping levels are identical. Accordingly, the fairly lower strain levels observed for the modified AZO structures could imply slightly enhanced crystallinity of their structures after the growth process, originating from less crystal lattice distortion and fewer numbers of defects such as grain-boundaries and porosities [24].

4.4. Electrical behavior of the films

Preliminary, the electrical performance of the TCO film directly depends on the concentration N and mobility μ of the charge carriers, which are in turn altered by the microstructural variations. This is confirmed by the result displayed in Table 4 about the electrical resistivity of the samples. Accordingly, after the final heat-treatment, resistivity values are around one order of magnitude smaller in AZO films of Group B compared with those of Group A ones; indicating that improved electrical conductivities are obtained through performing the high temperature approach of thermal treatment by which, structures with stronger c-axis oriented and greater $T_c(002)$ and $I_r(002)$ values are resulted. Besides, in both groups, fairly lower resistivity values are detected for the modified AZO films. However, the resistivity of undoped ZnO sample is not altered by the microstructural improvements.

These correlations could be associated to the polycrystalline nature of the films and the contribution of grain-boundaries in the charge carrier transport in terms of degrading the mobility of electrons and therefore, the conductivity of the films. Generally, the charge carrier transport in doped semiconductors is limited through three independent scattering mechanisms [82,83]; (1) the scattering by the host-lattice vibration; (2) the ionized scattering due to the distortion resulting from the presence of intrinsic and extrinsic carriers; and (3) the scattering caused by surface-defects. Higher values of mobility are expected for the undoped ZnO samples since the ionized scattering is less-frequent; unlike the AZO samples in which due to the huge numbers of carriers added through Al doping, the charge transport is accompanied by ionized scattering and therefore, lower mobility values are expected. Among the AZO samples, considering the impeding effect of the host-lattice

scattering being little at room temperature [18,83], and an identical ionized scattering due to the equal level of doping, the surface-defect scattering is the only reason for the difference observed in conductivity values. The surface-defect scattering is mainly caused by grain-boundaries and their effect on the electrical conductivity was explained by Seto [17] through defining the barrier model. Accordingly, the crystallographically disturbed surfaces between the grains contain a high density of defects and impose a surface-defect energy E_s to the structure as a direct function of the density and the surface energy of grain-boundaries. With respect to the electronic states, E_s is interpreted as localized electronic states within the band-gap with a density value correlated to the defects density. Since in n-type semiconductors the Fermi level is above the localized states [18,84], the localized states related to grain-boundaries are acceptors for the adjacent grains and trap charge carriers from the bulk of the grains. It leads to form (1) charged boundary surfaces; and also (2) the so-called charge "depletion-region" in the bulk of the grains near the boundaries and along them. The charged boundaries establish a potential barrier which impedes the charge transport across the grain-boundaries and also inside the bulk along the depletion-regions [82,83]. Consequently, the non-affected volume for high-mobility charge transport is expected to be larger for a microstructure with larger grains and narrower depletion-region [85].

This explanation justifies the increase in conductivity values of AZO samples in Group B compared with the Group A ones after the final heat-treatment. Since among the structures with relatively equal crystallite size, a mono-oriented structure contains less density of grain-boundaries, the higher (002) texture coefficients could bring about less restriction for charge transport by forming narrower depletion-regions and therefore, higher values of carrier mobility in Group B AZO samples. Moreover, in modified AZO films, the comparatively higher conductivity could be associated to moderately larger crystallite sizes and less microstrain values. For undoped ZnO samples however, the absence of adequate charge carrier concentration is the predominant reason of high resistivity, making the grain-boundary effect by far insignificant.

Another point concluded from Table 4 is the significant effect of thermal treatment atmosphere observed as the result of additional heat-treatment. Accordingly, the resistivity values of Group B samples decreases by nearly two orders of magnitude, even for the undoped ZnO one, which implies a noticeable change in the electronic band structure beyond the microstructural variations.

Together with extrinsic carriers imported to the ZnO lattice by Al^{3+} dopants, another part of carrier concentration is intrinsically supplied by the lattice point defects including oxygen vacancies V_O and interstitial zinc ions Zn_i [86]. While V_O and Zn_i act as donor states and are considered as the origin of n-type conductivity in undoped ZnO; the zinc ion vacancies V_{Zn} and the interstitial oxygen ions O_i act as acceptor states against the intrinsic conductivity. V_O is the by far most abundant point defect due to its much lower formation energy [87,88]; however, performing the final heat-treatment in air atmosphere promotes the chemisorption of acceptor oxygen molecules on the film surface, inside the pores and between the grain-boundaries. Similar to O_i, the oxygen chemisorption involves capturing electrons from the ZnO bulk located in the conduction band and formation of O^{-2} and O^- ions leading to the carrier concentration loss. Moreover, it helps charge depletion regions in the bulk which degrades the mobility of carriers as mentioned above [89]. Hence, the low partial pressure of oxygen during the additional heat-treatment could enhance both the concentration and mobility of carriers by giving rise to better desorption of oxygen from the structure [90,91]. By partial introducing of H_2 to the furnace, the additional heat-treatment continues under reducing atmosphere. It is reported that [92] hydrogen-treatment increases the ZnO intrinsic conductivity through accelerating the oxygen desorption and also by etching of small grains growing among larger ones, leading to reduced grain-boundary scattering. More importantly, hydrogen behaves as a shallow donor in the electronic band structure of ZnO [93], leading to charge carrier increase as well. These explanations justify the functionality of the low oxygen pressure and also the role of hydrogen-treatment in decreasing the intrinsic resistivity of the undoped ZnO sample of Group B by performing the additional heat-treatment.

For AZO samples, the effectiveness of the additional heat-treatment is beyond the advantages mentioned for the undoped ZnO sample and expanded to alter the condition of extrinsic carriers as

well, regarding the position of Al^{3+} ions in the ZnO lattice. In the hexagonal structure of ZnO, the O^{-2} and Zn^{2+} ions occupy the tetrahedral positions while all of the octahedral holes are empty, providing suitable space for interstitial Al^{3+}. But ideally and in order to add a free electron to the lattice, one Al^{3+} must substitute for one Zn^{2+} at a tetrahedral position, since in case of interstitial occupation of octahedral sites, it behaves as an acceptor and decreases the conductivity [94]. In an inclusive investigation through performing ^{27}Al NMR spectrometry on AZO powders [95], Damm et al. reported that while before the reductive annealing, the relative occupancy of Al^{3+} in octahedral positions is more or less equal to the tetrahedral ones, after the reduction annealing a dominant substitutional tetrahedral occupancy of Al^{3+} is observed. It was also confirmed by Momot et al. that upon the reductive annealing, a rearrangement of the Al^{3+} coordination in ZnO lattice happens by migration of the Al^{3+} ions at interstitial positions to the substitutional positions [96]. This "dopant activation" contributes to conductivity boost up by increment of active charge carriers.

4.5. Optical behavior of the films

Based on the Maxwell's equations, the interaction between a medium and the incident electromagnetic wave depends on the electrical and magnetic characteristics of the medium; or more precisely, on the electrical conductivity σ and permittivity ε as well as the magnetic permeability [97]. So regarding non-magnetic compounds with permeability of unit of value, including conventional TCOs, the optical behavior depends on whether the medium shows dielectric or conductive features. The distinction resides in the fact that in the former, just bound electrons exist while in the latter, moving free electrons as the charge carriers respond to the incident wave as well. This interaction depends on the concentration and mobility values of free electrons; indicating that, different optical behaviors are expected for samples of a certain compound with different N and μ and hence, different conductivity. Such correlation between the optical and electrical behaviors is confirmed by the results displayed in Table 5 as the summary of the observed values in Figures 5 to 7 for the optical properties of Group B samples after the additional heat-treatment. In the following, we discuss the effect of N and μ on the observed optical behavior in two forms of optical absorption and dispersion.

4.5.1. Absorption behavior

For high-energy photons of around 3 eV and above (equivalent with UV wavelengths of $\lambda \leq 400$ nm), the sharp reduction in the transmittance spectra in Figure 5(a) shows that the optical behaviors of the samples are dominated by the fundamental absorption occurring as excitation of electrons. In this range, as depicted in the inset of Figure 6(a), the absorption coefficient α shows two different relationships with the photon energy:

The first one, stated as Tauc empirical rule in Equation (7), is a parabolic relationship applied to the incident photons with energy levels higher than the band-gap energy ($E_g < E$); for which the eventual excitation of electrons happens as a direct "interband transition" from the valence to the conduction band. The E_g value for the band structure of a pure undoped ZnO single-crystal has been reported controversially ranging from 3.1 to 3.4 eV; but values above 3.3 eV are confirmed more frequently [41,81]. This is higher than the calculated E_g value of the undoped ZnO sample reported around 3.28 eV in Table 5. This "band-gap narrowing" is in accordance with previously reported data about ZnO thin films prepared by the sol-gel method on the quartz substrate [81,48] and it is associated with the existence of surface-defects. As mentioned in Section 4.4, due to being of small grain-size, there is a high density of surface-defects in form of grain-boundaries that create localized states within the band-gap and trap charge carriers from the bulk of the grains. It is reported that charged boundary surfaces decrease the E_g value [81,48]. So the absorption coefficient and E_g value of the undoped ZnO thin film sample is smaller than that of a single-crystal ZnO. On the other hand, there is an increase in the E_g values of AZO samples compared to the undoped ZnO one. This "band-gap widening" is reported to occur proportionally with increasing the free charge carriers through importing Al^{3+} dopants to the ZnO lattice [89]. As stated in Section 4.3, the substitution of smaller Al^{3+} with Zn^{2+} ions increases the compressive strain along the c-axis direction of AZO

samples; which is reported to cause band-gap widening compared with the undoped ZnO sample [80,81,98]. More importantly and based on the Moss–Burstein effect, doping generates donor levels at the base of the conduction band and increases the charge carriers through filling there with free electrons. Hereafter, the excited electrons from the valence band must overcome an additional energy gap to reach empty available states [43]. So a higher widening is expected for a larger concentration of free charge carriers N. Based on the difference in E_g values of Group B samples, we can conclude that N follows this trend: $N_{(ZnO)} \ll N_{(AZO\ 2\%)} \leq N_{(AZO2\%\ mod.)}$.

At the same time, the second relationship is an exponential one, introduced as Urbach empirical rule in Equation (8) for the photons with energy levels of $E < E_g$. It describes the transition of electrons in the localized states positioned within the band-gap and indicates the absorption of photon with energy levels even below the band-gap energy. The Urbach energy E_U characterizes the degree of absorption edge extension in to the sub-gap region and is related to the crystalline lattice disordering caused by the thermal vibrations and also crystallographic faults [45]. Thus, in a constant temperature, structural defects in the form of deviation from the perfect periodicity of an ideal crystalline state have the main contribution in increasing the width of absorption edge and observing higher Eu values [99]. With respect to electronic states, as it was mentioned in the Section 4.4, structural defects introduce localized electronic states within the band-gap, leading to the so called "tailing" of the states above the valence band and below the conduction band with an exponential distribution [84,100]. Therefore, while the band edges terminate abruptly in a defect-free single-crystalline structure and no optical absorption happens below the band-gap energy, in amorphous or microcrystalline and in heavily-doped structures, the localized band-tail states encroaching to the band-gap induce the optical absorption with an exponential dependency on the photon energy [101]. Here, E_U corresponds to the width of these localized states and informs about the overall effect of all types of lattice disorders such as strains, dislocations, porosities and most importantly grain-boundaries that form the trap states together [45,81]. To a minor extent, it is also associated with the fault originating from the remained organic molecules introduced to the system in the role of capping ligands [102]; as could be traced in the present study in Figure 3 in form of a pair of weak peaks related to CH_2 bond of MEA after thermal treatment at 600 °C. Since in ZnO as a n-type semiconductor the Fermi level is above the localized states [18,84], they act as the electron acceptor and can trap free electrons; so the charge transport is assumed as a series of trapping and release events regarding such electron traps. The density of these localized states is a determining factor in the electronic performance of a semiconductor in terms of reducing its charge carrier mobility μ; and it is found the density of localized states increases with increasing the E_U value [100]. So based on the difference in E_U values of Group B samples, we conclude that μ follows this trend: $\mu_{(AZO\ 2\%)} < \mu_{(AZO2\%\ mod.)} < \mu_{(ZnO)}$.

In addition to the transition of electrons, the fundamental absorption is also attributed to the formation of excitons. Excitons are bound-states between the excited electrons in the conduction band and the corresponding holes in the valence band stabilized through Coulomb force attraction. These excitonic states dominate the absorption above the absorption edge [103]. As observed in Figure 6(a), the undoped ZnO sample shows an excitonic peak at around 3.4 eV in the absorption coefficient spectrum α, coordinated with the peak at around 364 nm in the absorption index spectrum k of Figure 7(b). The excitonic peak is also correlated with a minimum in the transmittance spectrum in Figure 5(a), as a shoulder peak between 360 to 370 nm. However, the excitonic absorption peak is hardly observed for the AZO samples spectra, indicating that the so called "exciton Mott transition" is activated; whereby, the interaction of excitons with free electrons in the conduction band alters the electron-hole binding characteristics and results in exciton dissociation and therefore, broadening or total vanishing of the excitonic absorption peak [104-106]. The exciton Mott transition implies the existence of free electrons in the conduction band and having a degenerate semiconductor with metallic behavior [42,106]. Here, for both spectra of α and k, the broadening of excitonic peak in the modified AZO sample is detected slightly more intensive, so it may be concluded that a fairly higher density of free electrons in the conduction band of the

modified AZO sample causes more exciton dissociation and almost total vanishing of the peak, and hence, $N_{(ZnO)} \ll N_{(AZO\,2\%)} \leq N_{(AZO2\%\,mod.)}$.

For the photons with visible and IR wavelengths of around $400 \leq \lambda \leq 700$ nm and $\lambda \geq 700$ nm (possessing the energy levels of 1.6 to 3 eV and below 1.6 eV), the interband transition of bound electrons does not occur, as the incident photons cannot provide the required energy for the electron excitation. So principally no absorption behavior is expected in these ranges; however, the presence of free electrons in the conduction band and their response to the incident photons affects the optical behavior of a degenerate semiconductor compared to the non-degenerate one.

In the range of visible wavelengths, as depicted in Figure 5(a), the undoped ZnO sample exhibits a high average transmittance up to nearly 90% while the value drops to roughly 80% for the doped samples. The visible reflectance spectra in Figure 5(c) also depicts a clear distinction where average values for the doped samples are nearly 22% and 18% compared to 12% for the undoped ZnO one. On the other hand, the visible range of the absorptance spectra in Figure 5(d) is almost identical for all samples with average values below 1%. Insignificant visible absorption is also confirmed by the spectra of absorption coefficient α and absorption index k in Figure 6(a) and 7(b) respectively. This observation shows that the transparency loss in the visible range is mainly due to the reflection, and not because of the transition-based absorption of photons.

In the IR range, as depicted in Figures 5(a) and (b), samples are highly transparent as long as a sharp reduction in the transmittance occurs for all. However, the undoped ZnO sample keeps the transparency for a much broader wavelength interval compared to the doped ones. At the same time, on the far right of the absorptance spectra as illustrated in the inset of Figure 5(d), a new absorption trend of the so called "free carrier absorption" is observed to initiate only for the doped samples. The free carrier absorption is correlated to the increment of absorption coefficient for the low-energy photons in Figures 6(a) and 6(d), and is responsible for transmission loss in the IR range as illustrated in Figure 5(b). The free carrier absorption increases directly with the free carrier concentration N [107-109], as the larger value of N changes the onset and maximum wavelength of the absorptance spectrum with a blue shift [3]. The blue shift could be observed for the modified AZO sample in the inset of Figure 5(d) and also in Figure 5(b) supposing that the maximum absorptance happens roughly at the transmission minimum wavelength. Accordingly, through comparing Figures 5(b) and 5(d) it can be concluded that: $N_{(ZnO)} \ll N_{(AZO\,2\%)} \leq N_{(AZO2\%\,mod.)}$.

4.5.2. Dispersion behavior

The final argument on the samples optical behavior could be stated through the dispersion theory, which explains the frequency-dependent response of a medium to the incident wave from the optical and electrical point of view, in terms of refraction and relative permittivity function. Accordingly [110], the solid medium is considered as an arrangement of self-oscillating components embedded in vacuum. Their response to an incident electromagnetic wave is emitting wavelets with the same frequency as of the incident wave expanding in all directions; however wavelets interference is constructive just in one direction and destructive in other lateral directions. So a redirected secondary wave is formed and propagates in the medium. The emission of wavelets happens with a delay, so compared to the incident wave, the secondary wave has a phase-lag which reduces its amplitude. The phase-lag value of a single wavelet is related to the incident wave frequency ω, and also the medium oscillation resonance ω_r. The total phase-lag is the aggregate of all phase-lags formed by all components along propagation path, so it is proportional with the medium thickness. For a thin medium or when the incident wave is of very low-energy in which $\omega \ll \omega_r$, there is almost no delay in wavelet emission and the total phase-lag is nearly zero. In this condition, the secondary wave propagates through the medium with the same amplitude and frequency of the incident wave; which means that the medium is transparent. For a thick medium or when the incident wave is of higher energy, the phase-lag increases directly with the ω and thickness. In this condition, the secondary wave has the same frequency but less amplitude than that of the incident wave, indicating partial energy absorption and less transmission. Finally for an incident wave in

which $\omega = \omega_r$, or when the medium is thicker, the amplitude of the secondary wave becomes zero and the total absorption occurs.

Optically, the redirection of the secondary wave determines the refraction of light and the refractive index value n; and the amplitude reduction, resulted from the total phase-lag, associates with the absorption index k and therefore, the absorption coefficient α as stated in Equation (9). Figures 7(a) and 7(b) depict the refraction function of Group B samples. The k value in the visible region is nearly zero for all samples, following regular transparent semiconductors properties. However, in the infrared region as depicted in the inset of Figure 7(b), an increasing trend of k is observed for the doped samples unlike the undoped ZnO one, indicating the free carrier absorption as mentioned in 4.5.1 Section. Similarly, the blue shift of the onset wavelength in the modified AZO sample indicates a slightly higher value of free carrier concentration compared with the pure AZO one. On the other hand, since n is affected by the degree of crystallinity, it is possible to evaluate the density of defects through comparing the n values of the films with that of the bulk .Using Lorentz–Lorentz relation stated in Equation (10) [50-52] the porosity volume fraction is estimated as a basis to compare the films structural uniformity and thus, the carrier transport mobility. So according to the data reported in Table 5, μ follows such a trend: $\mu_{(AZO\ 2\%)} < \mu_{(AZO2\%\ mod.)} < \mu_{(ZnO)}$.

From the electrical point of view, the response of the medium to the oscillating electric field $\vec{E}$ of an incident electromagnetic wave in the optical frequency range is described by formation of oscillating electronic dipoles due to a slight shifting of the negative cloud of electrons from positive atomic nuclei. The summation of all dipole moments is the electronic polarization field $\vec{P}$, which has a phase delay compared to $\vec{E}$ and is related to it through the frequency-dependent parameter of electrical permittivity $\bar{\varepsilon}$ as $\vec{P} \sim \bar{\varepsilon}.\vec{E}$ [110]. Similar to refraction function, $\bar{\varepsilon}$ also is a complex function and comprises a real part ε indicating the degree to which the medium can be polarized and an imaginary component $\acute{\varepsilon}$ associated with the attenuation of electromagnetic wave passing through the medium [111]. Figures 7(c) and 7(d) compare the permittivity function of Group B samples. The samples demonstrate an almost a similar trend throughout the selected frequency (energy) region, with a maximum polarization around the band-gap energy as the equivalent for the resonance frequency of dipole oscillation. For the incident $\vec{E}$ of higher frequencies, the dipoles are no longer able to follow the oscillations and the electronic polarization stops, but the dipoles oscillation continues until being absorbed and attenuated by the structure. This time-dependent process is known as dielectric relaxation, which is evidenced by a drop in ε and a maximum in $\acute{\varepsilon}$ [112]. In spite the similar trend, it is observed that the undoped ZnO shows sharp peaks for both ε and $\acute{\varepsilon}$ spectra around the band-gap energy, while for the doped samples peak broadening and reduction of both ε and $\acute{\varepsilon}$ values occurs. In $\acute{\varepsilon}$ spectra, the undoped ZnO peak correlates with the excitonic absorption which is broadened for the doped samples under similar justification explained in Section 4.5.1. For ε, this observation is attributed to shorter dielectric relaxation, resulting from higher damping intensity against the dipoles oscillation [113]. The possible source for the damping of dipoles oscillation could be associated to the active electron scattering mechanisms. As stated in Section 4.4, in the undoped ZnO the ionized scattering is less frequent compared to the doped ones, which is claimed to cause collision-based damping [114]. Therefore, a higher level of damping and shorter relaxation time is concluded for AZO films. Considering the equal level of doping and thus, a nearly identical ionized scattering in AZO structures, difference in their peak broadening could be related to the damping originated from structural non-uniformity of grain-boundaries, as previously referred by surface-defect scattering [112]. This means that the lower peak broadening and damping intensity could be associated with less surface-defect scattering in the modified AZO compared with the pure AZO. The effect of grain size reduction on relaxation time shortening is also observed in other sol-gel derived systems [115]. The proposed comparison among damping intensity of the samples is in accordance with the calculated values for the damping energy Γ reported in Table 5 as $\Gamma_{(ZnO)} < \Gamma_{(AZO2\%\ mod.)} < \Gamma_{(AZO\ 2\%)}$. Eventually, assuming that $\bar{\varepsilon}$ is affected by the presence of free electrons and structural defects through their impact on the damping intensity, a qualitative estimation for the scattering time τ of electrons could be proposed by comparing dispersive behavior of $\bar{\varepsilon}$. The scattering time τ, which has inverse relationship with the damping as $\tau \sim 1/\Gamma$ is

considered as the average of the time intervals that an electron in the electric field is accelerated until it collides with other electrons or with structural defects that changes its energy. This parameter fundamentally associates with the concept of electron mobility by a direct relationship as $\mu \sim \tau$ [116]. Thus, we can conclude that μ follows such a trend: $\mu_{(AZO\ 2\%)} < \mu_{(AZO2\%\ mod.)} < \mu_{(ZnO)}$.

5. Conclusions

The polycrystalline nature and the grain-boundaries characteristics were determined as the most crucial factor influencing the electrical and optical properties of sol-gel derived ZnO thin films doped with 2 at.% Al.

The investigation was conducted to study the effects of sol chemistry and thermal treatment procedure. The sol chemistry was modified by altering the hydrolysis reaction through adding water with the molar ratio of [H_2O/ZAD] = 2. It was argued that a complex ion forms in the coating sol in which, the Zn^{2+} cores are coordinated by MEA molecules and acetate ions in a dimer structure. The addition of extra water increases the amount of free $(OH)^-$ as the hydrolysis agent and accelerates formation of hydroxide-based complexes owing to the highly basic condition provided by ratio of [MEA/ZAD] = 2. The deposition of thin films was conducted via dip coating of 15 layers with slow withdrawal speed of 2.5 cm/min under controlled condition to obtain the thinnest and most uniform layer after each deposition. The drying and annealing steps were performed under two different thermal treatment approaches of low- and high-temperature. For the former, 275 °C and 500 °C were selected as the intermediate steps and final cycle temperatures respectively; while for the latter, the selected temperatures were 430 °C and 600 °C respectively. Moreover, the high-temperature approach was followed by an additional heat-treatment step for 1 hour at 400 °C under the reducing atmosphere of Ar/H_2 flow.

The structural analysis of the films via XRD diffraction analysis showed that the thermal treatment in high-temperature approach brings about samples with grains of considerably stronger c-axis preferred orientation compared with those of obtained from the low-temperature one. This result indicates that the high-temperature approach provides a better separation of the decomposition and crystallization steps during the thermal evolution of the deposited gel; a claim which was confirmed through the TG-DTA measurement and FT-IR spectroscopy. Therefore, the energetically-preferred columnar morphology with higher Tc(002) and Ir(002) values develops less restrictedly through the high-temperature approach, due to being less disturbed with the release of organic residuals during the nucleation and growth of the grains. Moreover, as the second conclusion for this part, the fairly larger crystallite size and slightly less microstrain values in the modified AZO structures implies an enhanced structural crystallinity after the growth process, originating from less crystal lattice distortion and fewer numbers of defects such as grain-boundaries and porosities.

The 4-point probe evaluation of thin films electrical properties after the final heat-treatment showed that ρ values of the doped films were around one order of magnitude smaller through the high-temperature approach compared with the low-temperature one; a reduction from around 3 to 4 Ω.cm to less than 0.5 Ω.cm. But for the undoped ZnO film ρ value was not affected. Besides, among the doped films, ρ values of modified AZO films were detected fairly lower than the pure AZO ones. The obtained conclusions confirm the correlation between the grain-boundaries characteristics and the conductivity values. Providing that enough carrier concentration is supplied via doping, the stronger c-axis oriented morphology obtained through the high-temperature approach results in less density of grain-boundaries which consequently reduces the surface-defects scattering. Therefore, the increase of carriers' mobility is believed to improve the conductivity. Moreover, for the modified AZO film, the fairly larger crystallite size and slightly less microstrain value could provide better mobility and conductivity values compared with the pure AZO ones.

In addition to the high-temperature approach, an additional heat-treatment step performed under the reducing atmosphere of Ar/H_2 showed to have an extremely determining effect on the conductivity through decreasing the R_{sh} values by nearly two orders of magnitude; a reduction from around 0.4 to 0.5 Ω.cm to nearly 6 to 15 mΩ.cm. It was argued that while the low partial pressure of

oxygen helps in desorption of acceptor oxygen molecules chemisorbed on the surface-defects and eliminating the related acceptor states, the partial introduction of H_2 creates shallow donor states. Therefore, the intrinsic conductivity improves. In AZO samples, the extrinsic carriers are also affected by the reduction annealing, since a rearrangement of Al^{3+} coordination in ZnO lattice happens through the migration of Al^{3+} ions located in interstitial positions to the substitutional positions. So the reduction annealing leads to the "dopant activation" in terms of increasing the substitutional tetrahedral occupancy of Al^{3+} and therefore, contributes to conductivity boost up by increasing the active charge carriers.

Finally, the UV-Vis-NIR spectroscopy that was performed to study the absorption and dispersion behaviors of the films supported the higher mobility, and to a lesser extent, the concentration of charge carriers in the modified AZO film. From the results obtained for Eu values, n values and studying the dielectric relaxation, it was concluded that $\mu_{(AZO\ 2\%)} < \mu_{(AZO2\%\ mod.)} < \mu_{(ZnO)}$. At the same time, by investigation on the band-gap widening, excitonic transition and the free carrier absorption in NIR region, it was concluded that: $N_{(ZnO)} \ll N_{(AZO\ 2\%)} \leq N_{(AZO2\%\ mod.)}$. The obtained orders for N and μ are in accordance with the conductivity order of $\sigma_{(ZnO)} \ll \sigma_{(AZO\ 2\%)} < \sigma_{(AZO2\%\ mod.)}$.

Taking the optical transmission in to account, the figure-of-merit values showed the following order: $FoM_{(ZnO)} \ll FoM_{(AZO\ 2\%)} < FoM_{(AZO2\%\ mod.)}$, which indicates the enhanced performance of the modified film as a transparent conducting film.

Acknowledgments: We would like to acknowledge Prof. Sandra Dire for the contribution to this work. Also, we are pleased to thank Prof. Georg Pucker from Fondazione Bruno Kessler (FBK – FMPS) in Trento, for the measurements of the spectroscopic ellipsometry.

Conflicts of Interest: The authors declare no conflict of interest.

References

1. Lewis, B.G.; Paine, D.C. Applications and Processing of Transparent Conducting Oxides. *MRS Bull.* **2000**, *25*, 22–27.
2. Pasquarelli, R.M.; Ginley, D.S.; O'Hayre, R. Solution processing of transparent conductors: From flask to film. *Chem. Soc. Rev.* **2011**, *40*, 5406–5441.
3. Coutts, T.J.; Wu, X.; Mulligan, W.P.; Webb, J.M. High-performance, transparent conducting oxides based on cadmium stannate. *J. Electron. Mater.* **1996**, *25*, 935–943.
4. Haacke, G. New figure of merit for transparent conductors. *J. Appl. Phys.* **1976**, *47*, 4086–4089.
5. Jain, V.K.; Kulshreshtha, A.P. Indium-Tin-Oxide transparent conducting coatings on silicon solar cells and their "figure of merit." *Sol. Energy Mater.* **1981**, *4*, 151–158.
6. Gordon, R.G. Preparation and Properties of Transparent Conductors. *MRS Proc.* **1996**, *426*.
7. Gordon, R.G. Criteria for Choosing Transparent Conductors. *MRS Bull.* **2000**, *25*, 52–57.
8. Hu, L.; Hecht, D.S.; Grüner, G. Percolation in Transparent and Conducting Carbon Nanotube Networks. *Nano Lett.* **2004**, *4*, 2513–2517.
9. De, S.; Coleman, J.N. Are There Fundamental Limitations on the Sheet Resistance and Transmittance of Thin Graphene Films? *ACS Nano* **2010**, *4*, 2713–2720.
10. Sepulveda-Mora, S.B.; Cloutier, S.G. Figures of merit for high-performance transparent electrodes using dip-coated silver nanowire networks. *J. Nanomater.* **2012**, *2012*.
11. Stadler, A. Transparent Conducting Oxides—An Up-To-Date Overview. *Materials (Basel).* **2012**, *5*, 661–683.
12. Minami, T. Transparent conducting oxide semiconductors for transparent electrodes. *Semicond. Sci. Technol.* **2005**, *20*, S35–S44.
13. Minami, T. Present status of transparent conducting oxide thin-film development for Indium-Tin-Oxide

(ITO) substitutes. *Thin Solid Films* **2008**, *516*, 5822–5828.

14. Puetz, J.; Chalvet, F.N.; Aegerter, M.A. Wet chemical deposition of transparent conducting coatings in glass tubes. *Thin Solid Films* **2003**, *442*, 53–59.
15. Chen, Z.; Li, W.; Li, R.; Zhang, Y.; Xu, G.; Cheng, H. Fabrication of Highly Transparent and Conductive Indium–Tin Oxide Thin Films with a High Figure of Merit via Solution Processing. *Langmuir* **2013**, *29*, 13836–13842.
16. Choi, S.; Kim, K.-T.; Park, S.; Kim, Y.-H.; Choi, S.; Kim, K.-T.; Park, S.K.; Kim, Y.-H. High-Mobility Inkjet-Printed Indium-Gallium-Zinc-Oxide Thin-Film Transistors Using Sr-Doped Al2O3 Gate Dielectric. *Materials (Basel).* **2019**, *12*, 852.
17. Seto, J.Y.W. The electrical properties of polycrystalline silicon films. *J. Appl. Phys.* **1975**, *46*, 5247–5254.
18. Ghosh, S.; Sarkar, A.; Chaudhuri, S.; Pal, A.K. Grain boundary scattering in aluminium-doped ZnO films. *Thin Solid Films* **1991**, *205*, 64–68.
19. Ohyama, M.; Kozuka, H.; Yoko, T. Sol-Gel Preparation of Transparent and Conductive Aluminum-Doped Zinc Oxide Films with Highly Preferential Crystal Orientation. *J. Am. Ceram. Soc.* **2010**, *81*, 1622–1632.
20. Nishio, K.; Miyake, S.; Sei, T.; Watanabe, Y.; Tsuchiya, T. Preparation of highly oriented thin film exhibiting transparent conduction by the sol-gel process. *J. Mater. Sci.* **1996**, *31*, 3651–3656.
21. Calnan, S.; Tiwari, A.N. High mobility transparent conducting oxides for thin film solar cells. *Thin Solid Films* **2010**, *518*, 1839–1849.
22. Znaidi, L.; Illia, G.J.A.A.S.; Guennic, R. Le; Sanchez, C.; Kanaev, A. Elaboration of ZnO Thin Films with Preferential Orientation by a Soft Chemistry Route. *J. Sol-Gel Sci. Technol.* **2003**, *26*, 817–821.
23. Ohyama, M.; Kouzuka, H.; Yoko, T. Sol-gel preparation of ZnO films with extremely preferred orientation along (002) plane from zinc acetate solution. *Thin Solid Films* **1997**, *306*, 78–85.
24. Kuo, S.-Y.; Chen, W.-C.; Lai, F.-I.; Cheng, C.-P.; Kuo, H.-C.; Wang, S.-C.; Hsieh, W.-F. Effects of doping concentration and annealing temperature on properties of highly-oriented Al-doped ZnO films. *J. Cryst. Growth* **2006**, *287*, 78–84.
25. Chen, J.; Chen, D.; Chen, Z. Optimization of the process for preparing Al-doped ZnO thin films by sol-gel method. *Sci. China, Ser. E Technol. Sci.* **2009**, *52*, 88–94.
26. Bu, I.Y.Y. Effects of the pre-annealing temperature on structural and optical properties of sol–gel deposited aluminium doped zinc oxide. *Ceram. Int.* **2014**, *40*, 11941–11946.
27. Musat, V.; Teixeira, B.; Fortunato, E.; Monteiro, R.C.C. Effect of post-heat treatment on the electrical and optical properties of ZnO:Al thin films. *Thin Solid Films* **2006**, *502*, 219–222.
28. Shu-wen, X. A Study of Annealing Time Effects on the Properties of Al:ZnO. *Phys. Procedia* **2012**, *25*, 345–349.
29. Nehmann, J.B.; Ehrmann, N.; Reineke-Koch, R.; Bahnemann, D.W. Aluminum-doped zinc oxide sol–gel thin films: Influence of the sol's water content on the resistivity. *Thin Solid Films* **2014**, *556*, 168–173.
30. Guzman, G.; Dahmani, B. Transparent conducting sol–gel ATO coatings for display applications by an improved dip coating technique. *Thin Solid Films* **2006**, *502*, 281–285.
31. Lutterotti, L. Total pattern fitting for the combined size–strain–stress–texture determination in thin film diffraction. *Nucl. Instruments Methods Phys. Res. Sect. B Beam Interact. with Mater. Atoms* **2010**, *268*, 334–340.
32. Sharma, D.; Jha, R. Transition metal (Co, Mn) co-doped ZnO nanoparticles: Effect on structural and optical properties. *J. Alloys Compd.* **2017**, *698*, 532–538.

33. Meziane, K.; El Hichou, A.; El Hamidi, A.; Mansori, M.; Liba, A.; Almaggoussi, A. On the sol pH and the structural, optical and electrical properties of ZnO thin films. *Superlattices Microstruct.* **2016**, *93*, 297–302.
34. Bandyopadhyay, S.; Paul, G.K.; Roy, R.; Sen, S.K.; Sen, S. Study of structural and electrical properties of grain-boundary modified ZnO films prepared by sol–gel technique. *Mater. Chem. Phys.* **2002**, *74*, 83–91.
35. Shikha, D.; Mehta, V.; Sood, S.C.; Sharma, J. Structural and optical properties of ZnO thin films deposited by sol–gel method: effect of stabilizer concentration. *J. Mater. Sci. Mater. Electron.* **2015**, *26*, 4902–4907.
36. Smits, F.M. Measurement of Sheet Resistivities with the Four-Point Probe. *Bell Syst. Tech. J.* **1958**, *37*, 711–718.
37. Rietveld, G.; Koijmans, C. V.; Henderson, L.C.A.; Hall, M.J.; Harmon, S.; Warnecke, P.; Schumacher, B. DC conductivity measurements in the Van Der Pauw geometry. *IEEE Trans. Instrum. Meas.* **2003**, *52*, 449–453.
38. Borgogno, J.-P.; Pelletier, E. Determination of the extinction coefficient of dielectric thin films from spectrophotometric measurements. *Appl. Opt.* **2009**, *28*, 2895.
39. Gadallah, A.-S.; El-Nahass, M.M. Structural, Optical Constants and Photoluminescence of ZnO Thin Films Grown by Sol-Gel Spin Coating. *Adv. Condens. Matter Phys.* **2013**, *2013*, 1–11.
40. Dolgonos, A.; Mason, T.O.; Poeppelmeier, K.R. Direct optical band gap measurement in polycrystalline semiconductors: A critical look at the Tauc method. *J. Solid State Chem.* **2016**, *240*, 43–48.
41. Srikant, V.; Clarke, D.R. On the optical band gap of zinc oxide. *J. Appl. Phys.* **1998**, *83*, 5447–5451.
42. Segura, A.; Sánchez-Royo, J.F.; García-Domene, B.; Almonacid, G. Current underestimation of the optical gap and Burstein-Moss shift in CdO thin films: A consequence of extended misuse of α2-versus-hν plots. *Appl. Phys. Lett.* **2011**, *99*, 2–5.
43. Sernelius, B.E.; Berggren, K.-F.; Jin, Z.-C.; Hamberg, I.; Granqvist, C.G. Band-gap tailoring of ZnO by means of heavy Al doping. *Phys. Rev. B* **1988**, *37*, 10244–10248.
44. Urbach, F. The Long-Wavelength Edge of Photographic Sensitivity and of the Electronic Absorption of Solids. *Phys. Rev.* **1953**, *92*, 1324.
45. Studenyak, I. Urbach Rule in Solid State Physics. *Int. J. Opt. Appl.* **2014**, 8.
46. Poelman, D.; Smet, P.F. Methods for the determination of the optical constants of thin films from single transmission measurements: a critical review. *J. Phys. D. Appl. Phys.* **2003**, *36*, 1850–1857.
47. Guenther, K.H. Physical and chemical aspects in the application of thin films on optical elements. *Appl. Opt.* **2009**, *23*, 3612.
48. Bandyopadhyay, S.; Paul, G.K.; Sen, S.K. Study of optical properties of some sol–gel derived films of ZnO. *Sol. Energy Mater. Sol. Cells* **2002**, *71*, 103–113.
49. Bond, W.L. Measurement of the refractive indices of several crystals. *J. Appl. Phys.* **1965**, *36*, 1674–1677.
50. De, S.; Higgins, T.M.; Lyons, P.E.; Doherty, E.M.; Nirmalraj, P.N.; Blau, W.J.; Boland, J.J.; Coleman, J.N. Silver Nanowire Networks as Flexible, Transparent, Conducting Films: Extremely High DC to Optical Conductivity Ratios. *ACS Nano* **2009**, *3*, 1767–1774.
51. Livage, J.; Henry, M.; Jolivet, J.P.; Sanchez, C. Chemical Synthesis of Fine Powders. *MRS Bull.* **1990**, *15*, 18–25.
52. Livage, J.; Sanchez, C.; Toledano, P. Sol-Gel Synthesis of Metal Oxide Clusters and Colloids. *MRS Proc.* **1992**, *272*.
53. Jiménez-González, A.E.; Soto Urueta, J.A.; Suárez-Parra, R. Optical and electrical characteristics of aluminum-doped ZnO thin films prepared by solgel technique. *J. Cryst. Growth* **1998**, *192*, 430–438.

54. Ohya, Y.; Saiki, H.; Takahashi, Y. Preparation of transparent, electrically conducting ZnO film from zinc acetate and alkoxide. *J. Mater. Sci.* **1994**, *29*, 4099–4103.
55. Zhong, X.; Feng, Y.; Zhang, Y.; Lieberwirth, I.; Knoll, W. Nonhydrolytic Alcoholysis Route to Morphology-Controlled ZnO Nanocrystals. *Small* **2007**, *3*, 1194–1199.
56. Znaidi, L.; Soler Illia, G.J.A.A.; Benyahia, S.; Sanchez, C.; Kanaev, A. V Oriented ZnO thin films synthesis by sol–gel process for laser application. *Thin Solid Films* **2003**, *428*, 257–262.
57. Chakrabarti, S.; Ganguli, D.; Chaudhuri, S. Substrate dependence of preferred orientation in sol–gel-derived zinc oxide films. *Mater. Lett.* **2004**, *58*, 3952–3957.
58. Kamalasanan, M.N.; Chandra, S. Sol-gel synthesis of ZnO thin films. *Thin Solid Films* **1996**, *288*, 112–115.
59. Ohyama, M.; Kozuka, H.; Yoko, T.; Sakka, S. Preparation of ZnO Films with Preferential Orientation by Sol-Gel Method. *J. Ceram. Soc. Japan* **1996**, *104*, 296–300.
60. Hancock, R.D. The chelate effect in complexes with ethanolamine. *Inorganica Chim. Acta* **1981**, *49*, 145–148.
61. Sridaeng, D.; Jitaree, W.; Thiampanya, P.; Chantarasiri, N. Preparation of rigid polyurethane foams using low-emission catalysts derived from metal acetates and ethanolamine. *e-Polymers* **2016**, *0*.
62. Ishioka, T.; Murata, A.; Kitagawa, Y.; Nakamura, K.T. Zinc(II) Acetate Dihydrate. *Acta Crystallogr. Sect. C Cryst. Struct. Commun.* **1997**, *53*, 1029–1031.
63. Ishioka, T.; Shibata, Y.; Takahashi, M.; Kanesaka, I.; Kitagawa, Y.; T. Nakamura, K. Vibrational spectra and structures of zinc carboxylates I. Zinc acetate dihydrate. *Spectrochim. Acta Part A Mol. Biomol. Spectrosc.* **1998**, *54*, 1827–1835.
64. Yang, J.; Puchberger, M.; Qian, R.; Maurer, C.; Schubert, U. Zinc(II) complexes with dangling functional organic groups. *Eur. J. Inorg. Chem.* **2012**, 4294–4300.
65. Gómez-Núñez, A.; Alonso-Gil, S.; López, C.; Roura, P.; Vilà, A. Role of Ethanolamine on the Stability of a Sol–Gel ZnO Ink. *J. Phys. Chem. C* **2017**, *121*, 23839–23846.
66. Gómez-Núñez, A.; López, C.; Alonso-Gil, S.; Roura, P.; Vilà, A. Study of a sol–gel precursor and its evolution towards ZnO. *Mater. Chem. Phys.* **2015**, *162*, 645–651.
67. Znaidi, L. Sol-gel-deposited ZnO thin films: A review. *Mater. Sci. Eng. B Solid-State Mater. Adv. Technol.* **2010**, *174*, 18–30.
68. Znaidi, L.; Touam, T.; Vrel, D.; Souded, N.; Yahia, S.; Brinza, O.; Fischer, A.; Boudrioua, A. AZO Thin Films by Sol-Gel Process for Integrated Optics. *Coatings* **2013**, *3*, 126–139.
69. Boudjouan, F.; Chelouche, A.; Touam, T.; Djouadi, D.; Khodja, S.; Tazerout, M.; Ouerdane, Y.; Hadjoub, Z. Effects of stabilizer ratio on photoluminescence properties of sol-gel ZnO nano-structured thin films. *J. Lumin.* **2015**, *158*, 32–37.
70. Khodja, S.; Touam, T.; Chelouche, A.; Boudjouan, F.; Djouadi, D.; Hadjoub, Z.; Fischer, A.; Boudrioua, A. Effects of stabilizer ratio on structural, morphological, optical and waveguide properties of ZnO nano-structured thin films by a sol–gel process. *Superlattices Microstruct.* **2014**, *75*, 485–495.
71. Yahia, I.S.; Farag, A.A.M.; Cavas, M.; Yakuphanoglu, F. Effects of stabilizer ratio on the optical constants and optical dispersion parameters of ZnO nano-fiber thin films. *Superlattices Microstruct.* **2013**, *53*, 63–75.
72. Hosseini Vajargah, P.; Abdizadeh, H.; Ebrahimifard, R.; Golobostanfard, M.R. Sol–gel derived ZnO thin films: Effect of amino-additives. *Appl. Surf. Sci.* **2013**, *285*, 732–743.
73. Tari, O.; Aronne, A.; Addonizio, M.L.; Daliento, S.; Fanelli, E.; Pernice, P. Sol–gel synthesis of ZnO transparent and conductive films: A critical approach. *Sol. Energy Mater. Sol. Cells* **2012**, *105*, 179–186.

74. Zeleňák, V.; Vargová, Z.; Györyová, K. Correlation of infrared spectra of zinc(II) carboxylates with their structures. *Spectrochim. Acta Part A Mol. Biomol. Spectrosc.* **2007**, *66*, 262–272.
75. Palacios, E.G.; Juárez-López, G.; Monhemius, A.J. Infrared spectroscopy of metal carboxylates. *Hydrometallurgy* **2004**, *72*, 139–148.
76. Fujihara, S.; Sasaki, C.; Kimura, T. Crystallization behavior and origin of c-axis orientation in sol-gel-derived ZnO:Li thin films on glass substrates. *Appl. Surf. Sci.* **2001**, *180*, 341–350.
77. Fujimura, N.; Nishihara, T.; Goto, S.; Xu, J.; Ito, T. Control of preferred orientation for ZnOx films: control of self-texture. *J. Cryst. Growth* **1993**, *130*, 269–279.
78. Schuler, T.; Aegerter, M.A. Optical, electrical and structural properties of sol gel ZnO:A1 coatings. *Thin Solid Films* **1999**, *351*, 125–131.
79. Goebbert, C.; Gasparro, G.; Schuler, T.; Krajewski, T.; Aegerter, M.A. Influence of the Layer Morphology on the Electrical Properties of Sol Gel Transparent Conducting Oxide Coatings. *J. Sol-Gel Sci. Technol.* **2000**, *19*, 435–439.
80. Malek, M.F.; Mamat, M.H.; Sahdan, M.Z.; Zahidi, M.M.; Khusaimi, Z.; Mahmood, M.R. Influence of various sol concentrations on stress/strain and properties of ZnO thin films synthesised by sol–gel technique. *Thin Solid Films* **2013**, *527*, 102–109.
81. Srikant, V.; Clarke, D.R. Optical absorption edge of ZnO thin films: The effect of substrate. *J. Appl. Phys.* **1997**, *81*, 6357–6364.
82. Nomoto, J.; Inaba, K.; Kobayashi, S.; Watanabe, T.; Makino, H.; Yamamoto, T. Characteristics of Carrier Transport and Crystallographic Orientation Distribution of Transparent Conductive Al-Doped ZnO Polycrystalline Films Deposited by Radio-Frequency, Direct-Current, and Radio-Frequency-Superimposed Direct-Current Magnetron Sputter. *Materials (Basel).* **2017**, *10*, 916.
83. Nguyen, V.H.; Gottlieb, U.; Valla, A.; Muñoz, D.; Bellet, D.; Muñoz-Rojas, D. Electron tunneling through grain boundaries in transparent conductive oxides and implications for electrical conductivity: the case of ZnO:Al thin films. *Mater. Horizons* **2018**, *5*, 715–726.
84. Lormand, G. ELECTRICAL PROPERTIES OF GRAIN BOUNDARIES. *Le J. Phys. Colloq.* **1982**, *43*, C6-283-C6-292.
85. Srikant, V.; Sergo, V.; Clarke, D.R. Epitaxial Aluminum-Doped Zinc Oxide Thin Films on Sapphire: II, Defect Equilibria and Electrical Properties. *J. Am. Ceram. Soc.* **1995**, *78*, 1935–1939.
86. Look, D.C.; Coşkun, C.; Claflin, B.; Farlow, G.C. Electrical and optical properties of defects and impurities in ZnO. *Phys. B Condens. Matter* **2003**, *340–342*, 32–38.
87. Lany, S.; Zunger, A. Dopability, intrinsic conductivity, and nonstoichiometry of transparent conducting oxides. *Phys. Rev. Lett.* **2007**, *98*, 2–5.
88. Liu, L.; Mei, Z.; Tang, A.; Azarov, A.; Kuznetsov, A.; Xue, Q.-K.; Du, X. Oxygen vacancies: The origin of n -type conductivity in ZnO. *Phys. Rev. B* **2016**, *93*.
89. Tang, W.; Cameron, D.C. Aluminum-doped zinc oxide transparent conductors deposited by the sol-gel process. *Thin Solid Films* **1994**, *238*, 83–87.
90. Geistlinger, H. effects on the thin-film conductivity. **1992**.
91. Glemza, R.; Kokes, R.J. Chemisorption of Oxygen on Zinc Oxide. *J. Phys. Chem.* **1965**, *69*, 3254–3262.
92. Baik, S.J.; Jang, J.H.; Lee, C.H.; Cho, W.Y.; Lim, K.S. Highly textured and conductive undoped ZnO film using hydrogen post-treatment. *Appl. Phys. Lett.* **1997**, *70*, 3516–3518.
93. Van de Walle, C.G. Hydrogen as a Cause of Doping in Zinc Oxide. *Phys. Rev. Lett.* **2000**, *85*, 1012–1015.
94. Kemmitt, T.; Ingham, B.; Linklater, R. Optimization of Sol–Gel-Formed ZnO:Al Processing Parameters

by Observation of Dopant Ion Location Using Solid-State 27 Al NMR Spectrometry. *J. Phys. Chem. C* **2011**, *115*, 15031–15039.

95. Damm, H.; Adriaensens, P.; De Dobbelaere, C.; Capon, B.; Elen, K.; Drijkoningen, J.; Conings, B.; Manca, J. V; D'Haen, J.; Detavernier, C.; et al. Factors Influencing the Conductivity of Aqueous Sol(ution)–Gel-Processed Al-Doped ZnO Films. *Chem. Mater.* **2014**, *26*, 5839–5851.
96. Momot, A.; Amini, M.N.; Reekmans, G.; Lamoen, D.; Partoens, B.; Slocombe, D.R.; Elen, K.; Adriaensens, P.; Hardy, A.; Van Bael, M.K. A novel explanation for the increased conductivity in annealed Al-doped ZnO: An insight into migration of aluminum and displacement of zinc. *Phys. Chem. Chem. Phys.* **2017**, *19*, 27866–27877.
97. Jahani, S.; Jacob, Z. All-dielectric metamaterials. *Nat. Nanotechnol.* **2016**, *11*, 23–36.
98. Ghosh, R.; Basak, D.; Fujihara, S. Effect of substrate-induced strain on the structural, electrical, and optical properties of polycrystalline ZnO thin films. *J. Appl. Phys.* **2004**, *96*, 2689–2692.
99. Pejova, B. The Urbach–Martienssen absorption tails in the optical spectra of semiconducting variable-sized zinc selenide and cadmium selenide quantum dots in thin film form. *Mater. Chem. Phys.* **2010**, *119*, 367–376.
100. Wager, J.F. Real- and reciprocal-space attributes of band tail states. *AIP Adv.* **2017**, *7*.
101. O'Leary, S.K. An empirical density of states and joint density of states analysis of hydrogenated amorphous silicon: a review. *J. Mater. Sci. Mater. Electron.* **2004**, *15*, 401–410.
102. Nelson, C.A.; Zhu, X.Y. Reversible surface electronic traps in PbS quantum dot solids induced by an order-disorder phase transition in capping molecules. *J. Am. Chem. Soc.* **2012**, *134*, 7592–7595.
103. Muth, J.F.; Kolbas, R.M.; Sharma, A.K.; Oktyabrsky, S.; Narayan, J. Excitonic structure and absorption coefficient measurements of ZnO single crystal epitaxial films deposited by pulsed laser deposition. *J. Appl. Phys.* **1999**, *85*, 7884–7887.
104. Li, X.D.; Chen, T.P.; Liu, P.; Liu, Y.; Leong, K.C. Effects of free electrons and quantum confinement in ultrathin ZnO films: a comparison between undoped and Al-doped ZnO. *Opt. Express* **2013**, *21*, 14131.
105. Makino, T.; Tamura, K.; Chia, C.H.; Segawa, Y.; Kawasaki, M.; Ohtomo, A.; Koinuma, H. Optical properties of ZnO: Al epilayers: Observation of room-temperature many-body absorption-edge singularity. *Phys. Rev. B - Condens. Matter Mater. Phys.* **2002**, *65*, 1–4.
106. Schleife, A.; Rödl, C.; Fuchs, F.; Hannewald, K.; Bechstedt, F. Optical absorption in degenerately doped semiconductors: Mott transition or Mahan excitons? *Phys. Rev. Lett.* **2011**, *107*, 1–5.
107. Fujiwara, H.; Kondo, M. Effects of carrier concentration on the dielectric function of ZnO:Ga and In_2O_3:Sn studied by spectroscopic ellipsometry: Analysis of free-carrier and band-edge absorption. *Phys. Rev. B* **2005**, *71*, 075109.
108. Li, X.D.; Chen, T.P.; Liu, Y.; Leong, K.C. Evolution of dielectric function of Al-doped ZnO thin films with thermal annealing: effect of band gap expansion and free-electron absorption. *Opt. Express* **2014**, *22*, 23086.
109. Zheng, H.; Zhang, R.-J.; Li, D.-H.; Chen, X.; Wang, S.-Y.; Zheng, Y.-X.; Li, M.-J.; Hu, Z.-G.; Dai, N.; Chen, L.-Y. Optical Properties of Al-Doped ZnO Films in the Infrared Region and Their Absorption Applications. *Nanoscale Res. Lett.* **2018**, *13*, 149.
110. Baker-Jarvis, J.; Kim, S. The Interaction of Radio-Frequency Fields With Dielectric Materials at Macroscopic to Mesoscopic Scales. *J. Res. Natl. Inst. Stand. Technol.* **2012**, *117*, 1–60.
111. Andrade-Neto, A. V.; Andrade-Neto, A. V. Dielectric function for free electron gas: comparison between Drude and Lindhard models. *Rev. Bras. Ensino Física* **2017**, *39*.

112. Elissalde, C.; Ravez, J. Ferroelectric ceramics: Defects and dielectric relaxations. *J. Mater. Chem.* **2001**, *11*, 1957–1967.

113. Mandal, S.; Mullick, H.; Majumdar, S.; Dhar, A.; Ray, S.K. Effect of Al concentration in grain and grain boundary region of Al-doped ZnO films: a dielectric approach. *J. Phys. D. Appl. Phys.* **2008**, *41*, 25307.

114. Hamberg, I.; Granqvist, C.G.; Berggren, K.-F.; Sernelius, B.E.; Engström, L. Band-gap widening in heavily Sn-doped In 2 O 3. *Phys. Rev. B* **1984**, *30*, 3240–3249.

115. Prakash, T.; Ramasamy, S.; Murty, B.S. Influence of bias voltage on dielectric relaxation of nanocrystalline anatase TiO2 using modulus formalism. *J. Appl. Phys.* **2011**, *109*.

116. Romanyuk, V.; Dmitruk, N.; Karpyna, V.; Lashkarev, G.; Popovych, V.; Dranchuk, M.; Pietruszka, R.; Godlewski, M.; Dovbeshko, G.; Timofeeva, I.; et al. Optical and electrical properties of highly doped ZnO:Al films deposited by atomic layer deposition on Si substrates in visible and near infrared region. *Acta Phys. Pol. A* **2016**, *129*, A36–A40.